8-2016

Nanophotonics for dark materials, filters, and optical magnetism

Mengren Man
Purdue University

Follow this and additional works at: https://docs.lib.purdue.edu/open_access_dissertations

 Part of the Electromagnetics and Photonics Commons, Nanoscience and Nanotechnology Commons, and the Optics Commons

PURDUE UNIVERSITY
GRADUATE SCHOOL
Thesis/Dissertation Acceptance

This is to certify that the thesis/dissertation prepared

By Mengren Man

Entitled Nanophotonics for Dark Materials, Filters, and Optical Magnetism

For the degree of   Doctor of Philosophy

Is approved by the final examining committee:

KEVIN J. WEBB

DAN JIAO

MINGHAO QI

ZHIHONG CHEN

To the best of my knowledge and as understood by the student in the Thesis/Dissertation Agreement, Publication Delay, and Certification/Disclaimer (Graduate School Form 32), this thesis/dissertation adheres to the provisions of Purdue University's "Policy on Integrity in Research" and the use of copyrighted material.

KEVIN J. WEBB

Approved by Major Professor(s): _____

Approved by: V. Balakrishnan   06/22/2016

Head of the Department Graduate Program   Date

NANOPHOTONICS FOR DARK MATERIALS, FILTERS, AND

OPTICAL MAGNETISM

A Dissertation

Submitted to the Faculty

of

Purdue University

by

Mengren Man

In Partial Fulfillment of the

Requirements for the Degree

of

Doctor of Philosophy

August 2016

Purdue University

West Lafayette, Indiana

TABLE OF CONTENTS

LIST OF FIGURES

Figure   Page

Figure   Page

ABSTRACT

Man, Mengren. Ph.D., Purdue University, August 2016. Nanophotonics for Dark Materials, Filters, and Optical Magnetism. Major Professor: Kevin J. Webb.

Research on nanophotonic structures for three application areas is described, a near perfect optical absorber based on a graphene/dielectric stack, an ultraviolet bandpass filter formed with an aluminum/dielectric stack, and structures exhibiting homogenizable magnetic properties at infrared frequencies. The graphene stack can be treated as a effective, homogenized medium that can be designed to reflect little light and absorb an astoundingly high amount per unit thickness, making it an ideal dark material and providing a new avenue for photonic devices based on two-dimensional materials. Another material stack arrangement with thin layers of metal and insulator forms a multi-cavity filter that can effectively act as an ultraviolet filter without the usual sensitivity of the incident angle of the light. This is important in sensing applications where the visible part of the spectrum is to be removed, allowing detection of ultraviolet signals. Finally, achieving a magnetic material that functions at optical frequencies would be of enormous scientific and technological impact, including for imaging, sensing and optical storage applications. The challenge has been to find a guiding principle and a suitable arrangement of constituent materials. A lattice of dielectric spheres is shown to provide a legitimately homogenized material with a magnetic response. This should pave the way for experimental studies.

More specifically, a graphene stack is designed, fabricated and characterized. The structure shows strong absorption of light. Spectroscopic ellipsometry is used to obtain the complex sheet conductivity of graphene. Further modeling results establish the graphene stack as the darkest optical material, with lower reflectivity and higher per-unit-length absorption than alternative light-absorbing materials.

An optical bandpass filter based on a metal/dielectric structure is modeled, showing performance that is largely independent of the angle of incidence. Parametric evaluations of the reflection phase shift at the metal-dielectric interface provide insight and design information. Filter passbands in the ultraviolet (UV) through visible or longer wavelengths can be achieved by engineering the dielectric thickness and selecting a metal with an appropriate plasma frequency, as demonstrated in simulations.

A lattice of suitable dielectric particles is shown to fulfill the requirements for a magnetic optical material. Using Mie theory, the microscopic origin of the magnetic response is explicitly identified as being due to the magnetic dipole resonance of an isolated sphere. This provides a design basis, and dielectric and lattice requirements with candidate dielectrics that will allow magnetic materials to be designed and fabricated for optical applications are presented.

1. INTRODUCTION

1.1 Background

Nanophotonics is concerned with studying the interaction between electromagnetic waves and structures with feature size at the nanometer scale. Research in this subject has seen rapid growth since the late twentieth century. Furthermore, with the advent of metamaterials, it has created new opportunities for controlling light in the sub-wavelength regime and promises a wide range of applications from energy harvesting, imaging, to photonic circuitry.

Efficient absorbers of light is necessary for harvesting energy from light. Recent studies on graphene have shown that it exhibits extraordinarily efficient absorption of light as an atomically thin material. Its excellent properties as an electrical conductor could potentially allow extraction of electrical current, if charge separation can be achieved following the creation of electron-hole pairs under excitation from light. Hence, we investigate the effectiveness of accumulating the absorption from individual sheets of graphene ($\approx 2\%$) by stacking [1]. The result is the darkest optical material ever created.

Optical filters and mirrors are commonly created from a dielectric stack. Such structures are important in the detection of certain wavelengths of light and for creating mirrors. A periodic structure composed of a unit cell having two different dielectrics, the usual arrangement, has relatively strong sensitivity to the incident angle of the light [2–4]. When designed for normal incidence, this means the performance degrades as the angle of incidence moved from the normal direction, often a problem in applications. Furthermore, achieving suitable dielectric fir ultraviolet (UV) wavelengths may be a challenge. The use of an aluminum-dielectric stack allows

very thin layers to be used, which reduces the sensitivity to incident angle, and it turns out the aluminum has useful properties in the UV [5].

Another aspect receiving wide attention in nanophotonics research are opportunities for optical magnetism, which is necessary in the perfect imaging devices based on metamaterials. As is well known, natural materials do not exhibit magnetic properties at optical frequencies. Artificial metamaterials employ resonant structures to achieve a magnetic dipole moment at such high frequencies. The first successful design of such a resonant structure was the split-ring resonator (SRR), but efforts to push the conduction current-based magnetic response into the optical regime have remained unsuccessful [6]. While plasmonic nanostructures support circulating displacement current at higher frequencies, losses associated with metals can be prohibitive. An alternate approach is to use dielectric structures. Dielectric particles made from materials with large positive permittivity support strong magnetic dipole resonances in the scattering of plane waves at optical frequencies [7–9]. Using Mie theory [10–12], we analyze the scattering properties of dielectric spheres and identify a magnetic dipole resonance. This feature is found to exist in the homogenized response of a lattice that produces a homogenized permeability. Features in the homogenized permeability are found to correspond to the magnetic dipole resonance of individual particles, which will have far-reaching impact.

1.2 Thesis Outline

This thesis consists of five chapters, including the introduction and summary chapters. Chapter 2 presents the design, modeling, fabrication, and characterization of a light-absorbing structure based on multiple layers of alternating graphene and dielectric. The optical properties of graphene are modeled using the frequency-dependent complex conductance, which is determined with spectroscopic ellipsometry of chemical vapor deposition (CVD) of graphene transferred to quartz substrate. A new technique for analyzing data from ellipsometry is developed, which takes into con-

sideration the incoherent superposition of light reflected from the back side of the optically thick substrate. Results from experiment and modeling establishes the performance of graphene stacks as the darkest material, which could have applications in energy harvesting.

In Chapter 3, a design for a UV bandpass filter is presented. The filter is composed of a stack of alternating metal and dielectric layers, similar to the graphene stack presented in Chapter 2. Aluminum is identified as the material of choice for achieving a metallic response at ultraviolet frequencies. The multilayer structure behaves as a coupled Fabry-Pèrot cavity system whose resonant transmission can be designed to go beyond the visible wavelength, in the ultraviolet regime. The angle-insensitivity of the filter is derived from cancellation of contribution to phase shift by forward propagation with that by reflection. Such properties make the structure an efficient UV filter with minimal fabrication difficulties.

In Chapter 4, we identify the microscopic origins for optical magnetism in dielectric metamaterials. A magnetic metamaterial response requires the excitation of a significant magnetic dipole moment, and the underlying structure should produce strong optical scatter, which typically occurs at a resonance. Among candidate structures, metamaterials composed of purely dielectric materials show promise as low-loss optical media, as they are free from losses commonly associated with metallic or plasmonic components. Recent developments in dielectric metamaterials draw attention to aspects of homogenization, characterization of such metamaterials as homogeneous media with effective parameters such as permittivity and permeability. In the process, we also carried out an analysis of the microscopic origins of homogenized magnetic response in relation to the behavior of optical scatter from individual dielectric particles. The results allow us to revisit the issue with rigorous methods for homogenization and establish a criterion for uniquely extracting the effective permittivity and permeability.

Chapter 5 gives a concise summary of the research findings and accomplishments.

There are three appendices. In modeling these structures, existing theories were studied and original models were developed. These are included in the appendices. The theory for monochromatic plane wave propagation in a planar stratified medium was developed for modeling the graphene stack and the UV-filter. A model for extracting the sheet conductivity of atomically thin 2D material such as graphene and MoS_2 was established. This new model does not require the use of a wavelength-dependent physical model for refractive index n or permittivity ϵ for least square fitting, as is common in existing spectroscopic ellipsometry studies. The model also takes into account of the incoherent superposition of light due to reflections from an optically thick transparent substrate. The Nicolson-Ross-Weir method that extracts material properties from S-parameters was used extensively in the studies on magnetic effective medium.

2. ULTRA-DARK GRAPHENE STACK METAMATERIALS

We present a fabrication method to achieve a graphene stack metamaterial, a periodic array of unit cells composed of graphene and a thin insulating spacer, that allows accumulation of the strong absorption from individual graphene sheets and low reflectivity from the stack. The complex sheet conductivity of graphene from experimental data models the measured power transmitted as a function of wavelength and number of periods in the stack. Simulated results based on the extracted graphene complex sheet conductivity for thicker stacks suggest that the graphene stack reflectivity and the per-unit-length absorption can be controlled to exceed the performance of competing light absorbers. Furthermore, the electrical properties of graphene coupled with the stack absorption characteristics provide for applications in optoelectronic devices.

2.1 Introduction

Metamaterials have provided a new domain for optical materials with the promise of important functionality, suggesting new devices and performance not achievable with natural materials. Various spatial arrangements of nanostructured materials may prove important in solar energy harvesting, for example [13]. With small reflection and significant absorption per unit length, a material becomes dark. Dark materials could prove to be of great use in applications like photovoltaics, photodetectors, and stealth technology. Among the possible dark materials that have been studied

so far, such as black silicon [14] and nickel-phosphorus alloys [15], the performance of vertically aligned carbon nanotubes (VA-CNTs) has stood out [16]. Recently, a graphene sheet stack was proposed, and simulated results indicated that this dark material should have important properties [17]. The proposed graphene sheet stack is composed of graphene and a thin, nanometer-scale, spacer having dielectric properties similar to the background medium, free space for most applications. Those graphene stack simulations indicated that the graphene stack should be the darkest material. Here, we present experimental data from fabricated graphene stacks, along with related simulation results, that indicates a performance as a black material that surpasses that of VA-CNTs, thereby establishing graphene stacks as the darkest material known.

Monolayer graphene consists of a single layer of carbon atoms arranged in a hexagonal honeycomb lattice. It is well established that a single layer of graphene shows a significantly high absorption over a large range of wavelengths [1, 18]. This behavior is remarkable considering the fact that graphene is just one atomic layer thick. Our idea of making extremely thin dark materials is based on the understanding that the absorptive property of individual graphene layers can be retained and accumulated if they are stacked together with a finite distance between them. As we will show later, this blackness results from the property that the reflection from the stack can be made small by changing the properties of the spacer while the (controllable) per unit length absorption, mostly determined by graphene's absorption and spacer's thickness, remains high. Another interesting materials aspect is that the stack provides a means to achieve high absorption independent of wavelength. Placing a material (a graphene sheet) in a cavity allows control of absorption at the expense of bandwidth. This removal of the absorption-bandwidth constraint, means that it is possible to realize devices that draw upon this concept. For instance, it becomes possible to control the sensitivity of a photodetector by using a graphene stack without compromising speed or bandwidth - and the (equal) high electron and hole velocities allows high speed. It is worthwhile to mention that the graphene stack can be homogenized into

an effective medium and the graphene layers are electrically isolated so that there is no charge transport between layers. In this sense, the properties studied here are those of a homogenized spatial arrangement of graphene, but not of graphene. Furthermore, although the optical properties of graphene only have received extensive attention, the extraction of complex conductivity (with displacement current) has not yet been dealt with properly. In our work, we present a detailed extraction method, which in principle, carries over to the many other two-dimensional optical materials that are of current interest to the materials community.

Figure 2.1 shows the schematic of a graphene stack, which consists of multiple graphene layers and intervening dielectric support layers. We present a graphene stack fabrication method and describe its optical properties using both measurement data and calculations based on extracted complex sheet conductivity from ellipsometry data. This provides understanding of the physical transport in graphene. Based on an excellent match between the experiments and the simulated results, we describe the key parameters of a stack and discuss how they should be tuned to achieve a near perfect black material. This provides evidence that graphene stacks are the darkest material to date.

The optical properties of a graphene stack were recently studied in far-infrared and THz region [19], in relation to the influence of doping and number of graphene layers on the plasmonic properties of a periodically patterned disc array. In that work, the disc array was of interest as a notch filter, and a ribbon arrangement operates as a polarizer. Drude parameters for the graphene sheet were extracted from measurements for single and multiple sheets. In our work, a rigorous extraction procedure is used to determine the graphene sheet complex conductivity at each measurement wavelength, and this is used in the stack description. Also, the properties of a graphene-based Bragg stack, a 1D photonic crystal, were recently investigated [20].
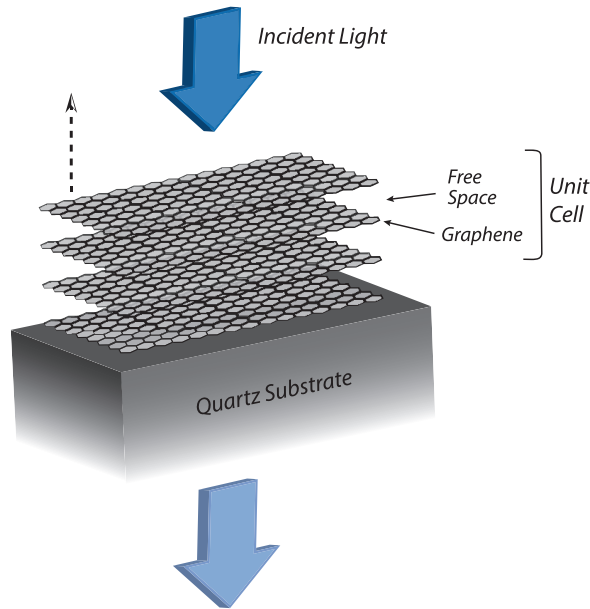
Fig. 2.1. Schematic of a graphene stack on a quartz substrate.

2.2   Fabrication of Graphene/PMMA Stack

We used CVD-grown graphene on copper foil with polymethyl methacrylate (PMMA) as a carrier for transfer [21, 22]. In this method, PMMA is spin coated over graphene grown on copper foil, and then the copper is removed by etching with a 1M $FeCl_3$ solution. The resultant graphene-PMMA layer was then transferred to a quartz substrate after rinsing it several times with water and HCl. Each period of a graphene-PMMA stack was fabricated using this process. The PMMA layer thickness can be controlled by changing its concentration as well as the spin speed, allowing tens to hundreds of nanometer film thicknesses to be achieved. This graphene transfer method is relatively straight forward, providing a viable and inexpensive way to produce thin dark materials. We fabricated the graphene-PMMA stack on a 0.5 mm thick quartz substrate (SPI# 01016T-AB) with each PMMA spacer of 200 nm thickness. Graphene (from Graphene Laboratories Inc.) was transferred from copper foil to quartz and before transferring the next unit cell, the substrate was baked at $180\,^\circ$C for 20 minutes

so as to allow the PMMA coating to soften and spread uniformly on the underlying graphene layer. This process can be repeated, yielding a periodic structure of graphene layers separated by PMMA.

2.3 Measurement of Sheet Conductivity of Graphene

To determine the graphene sheet conductivity, we transferred a single graphene-PMMA film to quartz, and then dissolved the PMMA using a hot acetone bath. Resides were removed by annealing in a forming gas environment (5% hydrogen and 95% nitrogen) at $500\,°$C for 30 minutes. Ellipsometry measurements were obtained (with a J. A. Woollam instrument) to extract the wavelength-dependent graphene film properties. The results of ellipsometry measurements are a result of superposition over the detector bandwidth. Such incoherent superposition causes no complication in thin film optics, as the phase difference accumulated between different wavelength components is negligible due to the small distance traversed by light. In such cases, light can still be modeled as monochromatic plane wave. However, it is inevitable to use a thick substrate (0.5 mm quartz) to support graphene, and as a result the reflected power varies drastically, even over a small wavelength range.

A rigorous extraction procedure was developed to adequately account for the incoherent superposition of light to represent the light source used in the ellipsometry measurements. It has been established that ellipsometry data can be expressed as functions of reflectance at four distinct polarizations $R(0°)$, $R(45°)$, $R(90°)$, and $R_\gamma(45°)$ where the angles in the argument refer to the orientation of the electric field vector with respect to the plane of incidence [23, 24]. Spectral averaging can be readily carried out for these reflectances. Given the optical thickness of the substrate ($n_{\text{quartz}} \times 0.5$ mm), the phase difference accumulated over the bandwidth of the light source is significantly larger than 2π. It is therefore sufficient to average these quantities over a phase of 2π as $\langle R(\alpha) \rangle = (2\pi)^{-1} \int_0^{2\pi} R(\alpha)\, \mathrm{d}\delta_n$, where δ_n is the phase accumulated via traversing the substrate, and $R(\alpha)$ is the unaveraged reflectance with

electric field making an angle α with the plane of incidence. We do not limit the frequency dependence of the sheet conductivity by the choice of a physical model (e.g., Lorentz, Cauchy, Drude), and instead carry out direct inversion of ellipsometry data to determine the wavelength-dependent complex sheet conductivity ($\sigma_s = \sigma'_s + i\sigma''_s$ [S]) for graphene. Details of the derivation of this extraction method can be found in the supporting information.

The extracted sheet conductivity is plotted in Fig. 2.2. Note that the conduction current dominates the displacement current, and that there is substantial dispersion, with increasing conductivity as the wavelength is reduced. Raman spectroscopy measurements were carried out on the same CVD-grown graphene transferred on a SiO_2(90 nm)/Si(0.5 mm) substrate. The defining feature of the Raman spectrum of graphene (as shown in the inset of Fig. 2.2) is the 2D peak. This peak is caused by a double resonance process due to electron scattering by two inter-valley transverse optical phonons [25]. The line-width of the 2D peak increases with increasing number of graphene layers due to coupling between them and a value of 45 cm^{-1} indicates that the sample largely consists of bilayer graphene [26]. We suspect that the dispersion in the wavelength range shown is due to impurities carried by graphene during the transfer process. We also show the universal graphene conductance [1, 27, 28] result [$\pi e^2/(2h)$, with e the electron charge and h Planck's constant] in Fig. 2.2. Note that the real part of the extracted conductance approaches this for longer wavelength, near-infrared light. The increasing σ at shorter wavelengths indicates that the absorption of graphene increases with reduction in wavelength, which is in agreement with previous reports of the excitonic peak shown by graphene in the UV range ($\sim$ 270 nm) [18].

2.4 Modeling the Optical Properties of Graphene/Dielectric Stacks

The optical modeling of the graphene/dielectric stacks was based on the transfer matrix method, which allows cascading of planar elements by multiplication of the
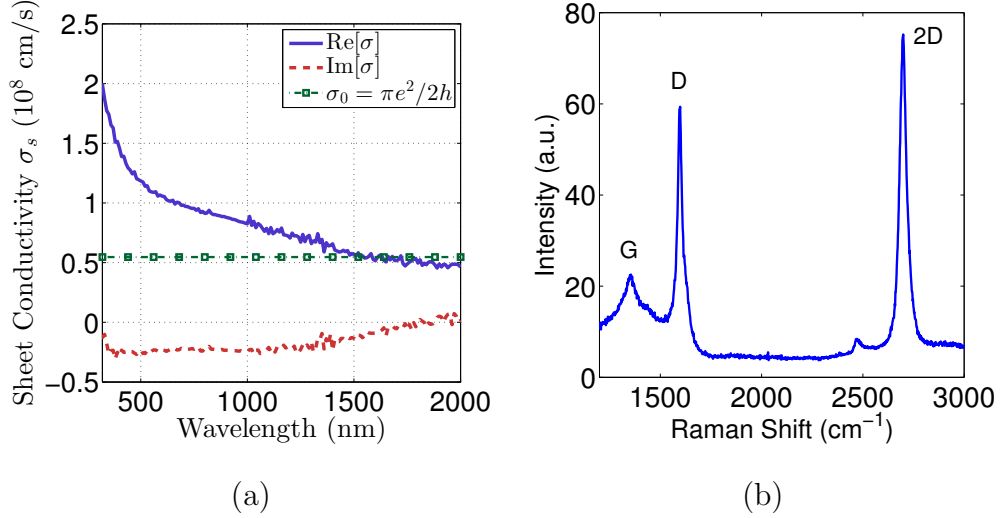
Fig. 2.2. (a) Conductance of CVD-grown bilayer graphene extracted from ellipsometry measurements (with $\exp(-i\omega t)$ time convention) plotted in the cgs-Gaussian unit of cm/s. Also shown (in green squares) is the constant theoretical conductance value for monolayer graphene [1]. (b) Measured Raman spectrum for the graphene sample with a 532 nm laser. The line-width of the 2D peak increases with increasing number of graphene layers, due to coupling between them, and a value of 45 cm^{-1} indicates that the sample largely consists of bilayer graphene [26].

corresponding element transfer matrices. The model uses a monochromatic plane wave having a definite direction of propagation/incidence. The transfer matrix for the graphene layer was modeled by a sheet conductivity. For comparison with experimental data, in which an optically thick substrate was present (Fig. 2.3), spectral averaging was carried out. The transfer matrix [29] for a graphene sheet having zero thickness is derived in the supplementary material. We carried out transmittance measurements on the graphene-PMMA stack after each unit cell transfer using a Perkin Elmer Lambda950 spectrophotometer. Experimental and simulated results at normal incidence are plotted in Fig. 2.3. Simulated results are spectrally averaged over a bandwidth representative of the measurements, which gives smooth spectra. An excellent agreement between the experimental and the predicted data validates our ellipsometric extraction of σ_s as well as the matrix model for the stack.
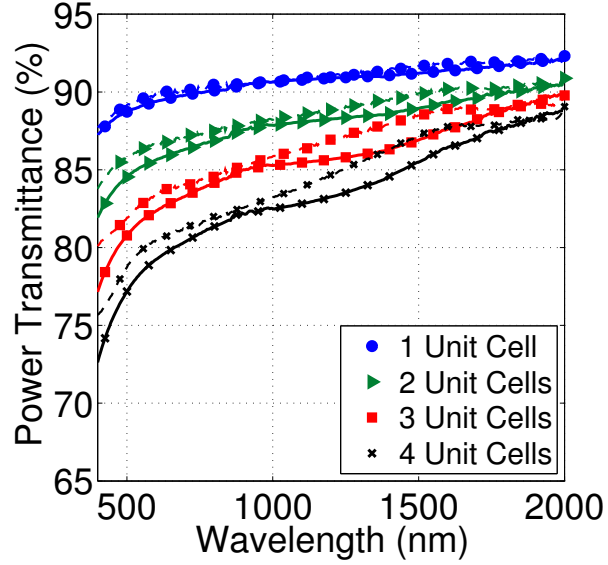
Fig. 2.3. Normalized measured transmitted power (thick-solid lines) at normal incidence for a graphene-PMMA stack with a spacer thickness of 200 nm and corresponding calculated values using the extracted graphene sheet conductivity (thin-dashed lines).

As the graphene-PMMA stack is extended to a higher number of unit cells, high absorption of light can be achieved with an overall stack thickness at the micron level. For 100 unit cells, such a stack absorbs almost 95% of light in the entire visible range and the per unit length absorption constant, α, of this graphene-PMMA stack is calculated to be 0.17-0.25 μm^{-1} (Over 700-400 nm, respectively). This property could prove to be beneficial in making inexpensive dark materials for small wavelength range when used with anti-reflection coatings (with an optimized thickness and impedance). With the recent introduction of large area CVD synthesis of graphene films and use of flexible thermal release tapes [30], the process of graphene transfer has become much faster, making multiple transfers easier.

Further improvement in the dark behavior of a graphene stack system requires reduction in reflectivity. As the reflectivity is strongly influenced by the refractive index of the spacer material, lowering the spacer refractive index can substantially

reduce the reflected power. Ideally, the graphene layers would be suspended in air. However, because a structural support is required, we desire a material with a refractive index close to 1. Materials with such a low refractive index do not exist in nature, so they have to be engineered as a homogenized effective medium. Typically, they can be made by introducing porosity in a bulk material so as to achieve a reduced effective refractive index. Such a material could be patterned with UV lithography for large scale manufacture. Here, we demonstrate a new e-beam lithography technique to make a pillared structure of hydrogen silsesquioxane (HSQ) (Fig. 2.4), a negative e-beam resist having a bulk refractive index of ~ 1.4, which can be used as a spacer in a graphene stack. In order to make the HSQ pillar array, we used a modified lithography technique that we call beam-hopping. Instead of exposing several circular patterns with short exposure times using a small step size within each pillar, we make the pattern using long exposure times and long step sizes, so that each individual beam exposure makes one of the pillars. After one long exposure, at a pillar location, the beam hops to the next pillar position. This technique significantly reduces the total lithography time, relative to conventional e-beam lithography. Figures 2.4(a) and (b) show the SEM and the AFM images, respectively, of an HSQ pillar array fabricated using this technique. The diameter of each pillar is 60 nm and the center-to-center distance between the pillars is 120 nm. An AFM scan across the edge of the sample gives a thickness of 118 nm for the HSQ layer. Ellipsometry measurements were carried out on this pillared structure at several angles of incidence to determine the effective refractive index. The refractive index of the HSQ layer was fitted to a Cauchy model [31], and was found to be approximately 1.04. With such a low refractive index, dispersion with wavelength is negligible. We also measured negligible depolarization in the light scattered from the pillar array.

Using the extracted complex sheet conductivity, we model the optical properties of a graphene stack having a spacer material of refractive index 1.04. For 50 unit cells, the absorption constant, α, and power reflectance, R, are plotted in Figs. 2.5(a) and (b), respectively, against spacer thickness and wavelength. As the spacer thickness
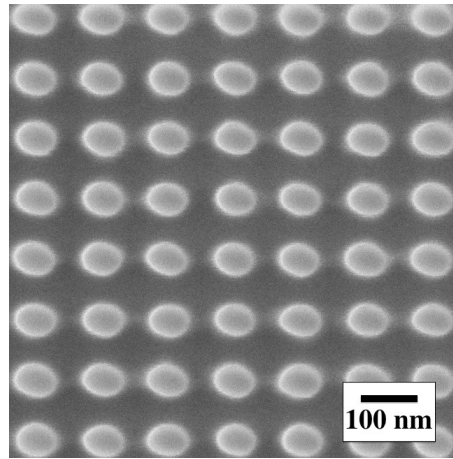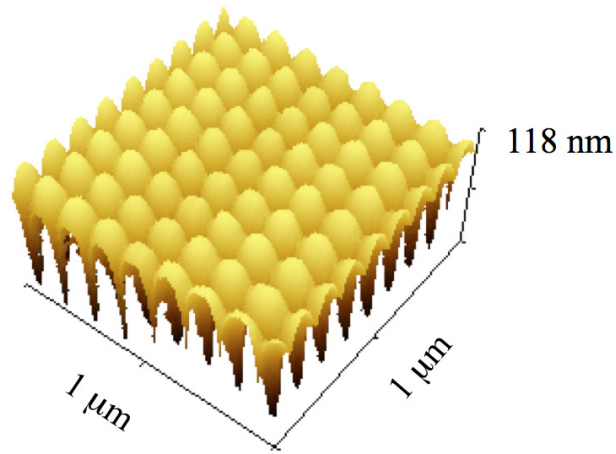
Fig. 2.4. (a) SEM and (b) AFM images of an HSQ pillar array, as a realization of an artificial low-index material for a graphene stack. The diameter of each pillar and the neck width are 60 nm, and the height is 118 nm. The refractive index of this pillared structure was found to be 1.04 using ellipsometry.

decreases, the conductivity of individual graphene layers start to add linearly, thereby resulting in the increased reflectance in this regime in Fig. 2.5(b). R is less than 0.05% for spacer thicknesses over 40 nm, but it increases sharply at smaller spacer thicknesses. Although α decreases monotonically with increasing spacer thickness, it remains large even when the spacer is more than 40 nm thick. A good compromise

between reflectivity and per unit length absorption suggests a spacer thickness of greater than 40 nm. The graphene stack thus gives an extremely low power reflectance with a very high per unit length absorption constant (implying a small total film thickness), the two characteristics which define the blackness of a material.
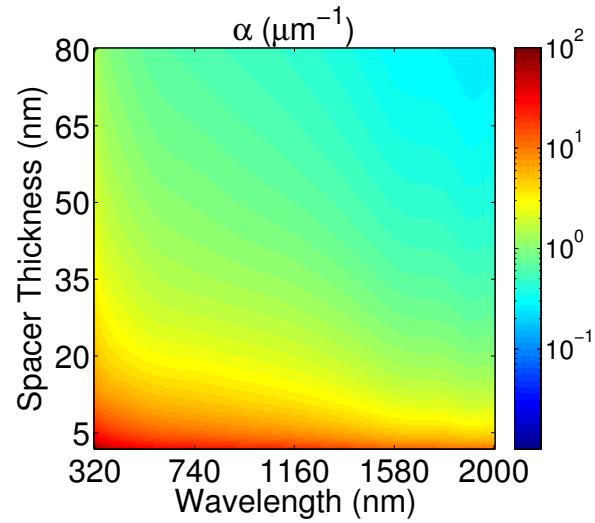
(a)
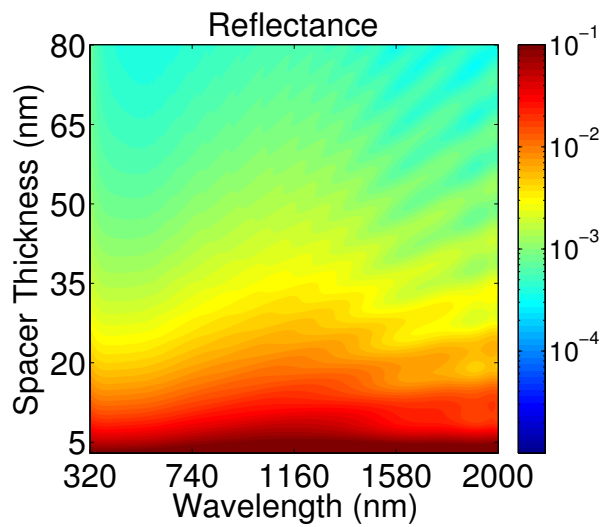
(b)

Fig. 2.5. (a) Calculated per unit length power absorption constant, α. (b) Power reflectance (normalized to 1) for a stack with 100 unit cells. The spacer has $n = 1.04$, and its thickness varies from 3 nm to 80 nm. In the quasistatic limit (spacing less than about 5 nm), where retardation effects over the stack is negligible, the conductance of individual graphene sheets adds linearly.

We find that these results for a low-index graphene stack are much better than those for VA-CNTs [16], in terms of both per unit length power absorption constant, α, and power reflectance, R. Optical measurements carried out on a carbon nanotubes array 300 μm in thickness showed $\alpha \approx 0.12$ μm^{-1} for light traveling along the carbon nanotubes. For a graphene stack having 50 unit cells with a spacer thickness of 75 nm (yielding a total thickness of ~ 38 μm) and spacer refractive index of 1.04, we find that $\alpha = 0.53$ μm^{-1} for normal incidence, more than 3 times that achieved with VA-CNTs. For the same stack, at normal incidence, the power reflectance is $R \approx 0.043\%$ at both 633 nm and 457 nm, while the corresponding values achieved for VA-CNTs are 0.045% and 0.07%. This suggests that graphene stacks show better performance than VA-CNT with even smaller thickness. The reflectivity of VA-CNTs can be controlled by changing the nanotube thickness and spacing, to change the effective refractive index. However, the ability to control the reflection by changing the spacer thickness in a graphene stack is important in increasing blackness by reducing reflection, and cannot be replicated with VA-CNTs.

An ideal black material should absorb light at all wavelengths, independent of the angle of incidence. It is therefore important to study the angle-dependent behavior of these graphene stacks. In order to further substantiate their potential as black materials, we plot the angle-dependent per unit length absorption constant and power reflectance spectra of the low-index stack consisting of 50 unit cells. Figure 2.6 shows the predicted absorption constant and power reflectance for TE and TM polarizations, respectively. It can be seen that the performance of the stack is extremely good even for large angles of incidence.

The combination of strong optical absorption over a wide wavelength range and high mobility carrier transport in graphene enables a wide range of optoelectronic applications, such as a new class of high speed photodetectors. Graphene, brought into contact with metals, naturally forms a potential barrier that can be tuned by electric field or chemical doping. While photo response of 0.001 A/W has been demonstrated in single layer graphene [32], our stacked graphene will maximize the photo absorp-
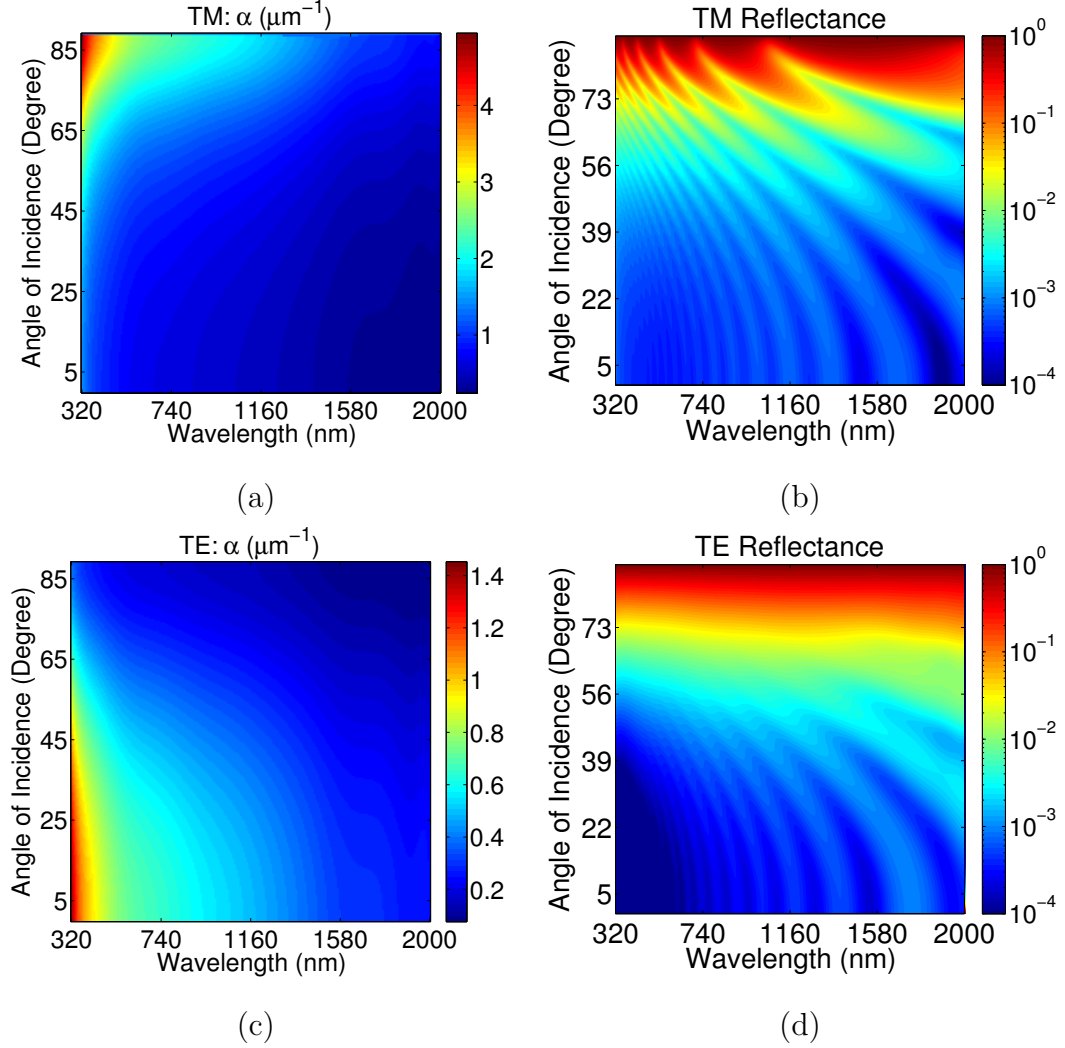
Fig. 2.6. Angle-dependent per unit length power absorption constant, α, and power reflectance (normalized to 1) spectra for a stack of 50 unit cells. The spacer has n = 1.04 and a thickness of 75 nm. (a), (b): Absorption constant and power reflectance, respectively, for TM incidence; (c), (d): absorption constant and power reflectance, respectively, for TE incidence.

tion and increase the photo response by two orders of magnitude, enabling ultrafast photodetectors. Recent work on graphene [33] shows that because of its small electron heat capacity and weak electron-phonon coupling, it can be used to make highly sensitive and fast bolometers that work at low temperatures. Our proposed graphene stack could be implemented as the absorbing material in such devices, thereby increas-

ing their sensitivity. The absorption ability of graphene in the microwave range [34] makes the graphene stack an ideal candidate for use in military applications as well. Highly absorbing graphene stack can be used as a radar absorbent material (RAM), improving stealth technology.

2.5   Conclusion

To conclude, we have demonstrated a graphene stack that has the characteristics of the darkest known material. The model developed provides a quantitative measure of the performance of these stacks and, furthermore, given a certain absorption/reflection requirement, helps us define their parameters, i.e. the refractive index and thickness of the spacer and the number of unit cells. As the darkness of these stacks critically depends on the spacer material, newer technologies to make low refractive index materials, which are cheaper and simpler, could prove to be beneficial. This, we believe, is the next step in the realization of darker metamaterials.

3. ANGLE-INSENSITIVE ULTRAVIOLET FILTERS BASED ON METAL-INSULATOR STACKS

We present a metal-dielectric stack ultraviolet (UV) bandpass filter that rejects the longer wavelength, visible spectrum and is thin and relatively insensitive to the angle of incidence. Parametric evaluations of the reflection phase shift at the metal-dielectric interface provide insight and design information. This non-trivial phase shift allows coupled Fabry-Pérot resonances with subwavelength dielectric film thickness. Furthermore, the total phase shift, with contributions from wave propagation and non-trivial reflection phase shift, is insensitive to the angle of incidence. Filter passbands in the UV can be shifted to visible or longer wavelengths by engineering the dielectric thickness and selecting a metal with an appropriate plasma frequency.

3.1 Introduction

Filters that pass a portion of the ultraviolet (UV) spectrum and reject longer wavelength visible light, making them solar blind, are important in sensing applications. Such filters could be used for flame sensing, in the detection of biological and chemical agents, and for plume detection. Furthermore, in such sensing and detection applications, it is important to have the same spectral response for a broad range of incident angles, i.e., angular-insensitivity [2].

Several types of UV filters have been proposed and demonstrated [3,4]. A solar blind UV band-pass filter consisting of a metal nano-grid was demonstrated by coating 20 nm of Al on a prefabricated SiO_2 square grid with a 190 nm period, 30 nm

linewidth, and 250 nm depth [4]. This coating process requires oblique deposition, which results in nonuniformity over the structure, and also the fabrication of a SiO_2 square nano-grid is rather complicated. The peak power transmission efficiency of about 27 % at normal incidence is further reduced by half by tilting the illumination angle to 20°. A multilayer dielectric stack consisting of high and low refractive index layers has also been demonstrated as a UV filter [3]. However, the multilayer dielectric stack, which utilizes the multiple interference effect from each layer, requires a thick stack and hence can be expensive to manufacture. Also, optical filters based on multiple interference are usually very sensitive to the angle of incidence, because the phase shift accumulated by light traversing the structure determines the resonance; the phase accumulation by propagation is intrinsically angle-sensitive. As a result, the transmitted power and hence filter response is strongly angle-dependent [35].

Metal-dielectric multilayer structures have been considered for bandpass filters in the visible regime, with normal incidence [36, 37], and when local homogenization is possible, as an equivalent ladder network at normal and oblique incidence [38]. Light can be transmitted into bulk metal, subject to the skin depth. However, by alternating thin metal and dielectric layers, high transmission is possible. The total thickness of this type of filter is small compared to all-dielectric interference filters. Other research has suggested an omnidirectional resonance can be supported in a metal-dielectric-metal (MDM) structure for TM light, in which the angular dependence of the propagation phase shift is (possibly partially) compensated by that of incident angle-dependent reflection phase shift at the dielectric-metal interface, resulting in angle-insensitivity [39]. This concept has been extended for the omnidirectional MDM single cavity Fabry-Pérot filter at visible regime [40].

In this Letter, we demonstrate an angle-insensitive and solar-blind UV bandpass filter based on a multilayer stack of metal and lossless dielectric films. We begin by evaluating the degree of non-trivial phase shift parametrically, and present a complete phase shift map for filter design and choice of material. The phase shift at the metal-dielectric interface allows the reduction of the length of each Fabry-Pérot cavity to tens

of nanometers, and introduces an angular insensitivity to the filter. By controlling the dielectric thickness and using metals with appropriate plasma frequencies, it is possible to implement a variety of bandpass filters whose central resonant wavelengths range from UV through visible or even longer wavelengths.
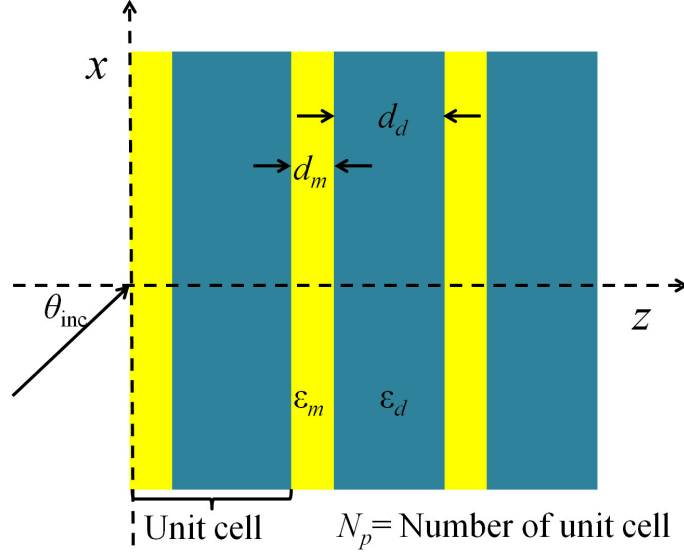
Fig. 3.1. Schematic of the metal-dielectric multilayer filter structure: d_m and d_d are the metal and dielectric thicknesses, respectively, ϵ_m and ϵ_d are, respectively, the dielectric constants of the metal and dielectric, N_p is the number of unit cell periods, and θ_{inc} is the angle of incidence.

Figure 3.1 shows a schematic of the metal-dielectric multilayer structure, with the corresponding parameters. Here, d_m and d_d are the metal and dielectric thicknesses, respectively, ϵ_m and ϵ_d are, respectively, the dielectric constants of the metal and dielectric, N_p is the number of unit cell periods, and θ_{inc} is the angle of incidence. The transfer matrix method (TMM) [29] was used to calculate the normalized transmission (T) and reflection (R) power spectra, and the normalized absorption (A) power spectrum was obtained from $A = 1 - T - R$. We use Al [41] and SiO$_2$ [5] as the metal and dielectric, respectively. Unlike commonly used plasmonic metals, such as Ag and Au, the plasma frequency for Al (3.57×10^{15} Hz or 79.7 nm) lies deep in the

UV region. While in the visible regime Al has high loss, that in the UV is low, making it a good plasmonic material in this wavelength range. Furthermore, the smaller real part of the dielectric constant in the UV facilitates film transmission.

3.2 Non-trivial Phase Shift
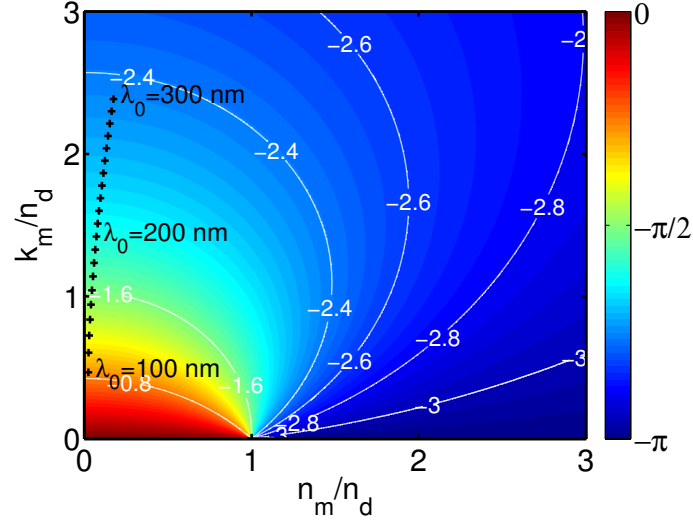
Fig. 3.2. Calculated reflection phase shift as a function of normalized (by $n_d = 1.5$) real (n_m/n_d) and imaginary (k_m/n_d) metal refractive index under normal incidence. The black plus symbols show the trajectory for Al as a function of free space wavelength.

To understand better the material conditions for controlling the cavity phase, we evaluated the electric field reflection phase shift $(\phi_{\rm ref})$ at the interface of a lossless dielectric (refractive index $n_d = \sqrt{\epsilon_d}$) and a semi-infinite metal $(\tilde{n}_m = n_m + ik_m = \sqrt{\epsilon_m})$, under normal incidence, which is given by

$$\Gamma_{\rm n} = \frac{n_d - (n_m + ik_m)}{n_d + (n_m + ik_m)} \tag{3.1}$$

$$\phi_{\rm ref}\left(\Gamma_{\rm n}\right) = \arctan\left[\frac{-2\left(\frac{k_m}{n_d}\right)}{1 - \left(\frac{n_m}{n_d}\right)^2 - \left(\frac{k_m}{n_d}\right)^2}\right], \tag{3.2}$$

where $-\pi \leq \phi_{\mathrm{ref}}(\Gamma_\mathrm{n}) \leq 0$. Γ_n is the reflection coefficient at the metal-dielectric interface with a normal illumination, and $\phi_{\mathrm{ref}}(\Gamma_\mathrm{n})$ is the phase component of Γ_n. In Fig. 3.2, we plot $\phi_{\mathrm{ref}}(\Gamma_\mathrm{n})$ using Eq. (C.2) as a function of n_m/n_d and k_m/n_d; the real (n_m) and imaginary (k_m) components of metal refractive indices are normalized by the adjacent lossless dielectric (n_d). Calculations show that the phase shift approaches $-\pi/2$ as the denominator of Eq. (C.2) approaches 0, i.e., $1-(n_m/n_d)^2-(k_m/n_d)^2 \to 0$. The case for Al is also plotted as a function of wavelength (black plus symbols) in Fig. 3.2. Here, the refractive index of the lossless dielectric is chosen to be $n_d = 1.5$, that assumed for SiO$_2$. Notice that over the free space wavelength range of 150 nm to 300 nm, the reflection phase shift at the SiO$_2$-Al interface is quite high ($-3\pi/4 \leq \phi_{\mathrm{ref}}(\Gamma_\mathrm{n}) \leq -\pi/2$), and therefore we consider implementing this wavelength region as the resonant filter passband. In such a spectral region, the resonant cavity length can be reduced, suppressing the phase accumulation by wave propagation.

3.3   Modeling the UV-Filter
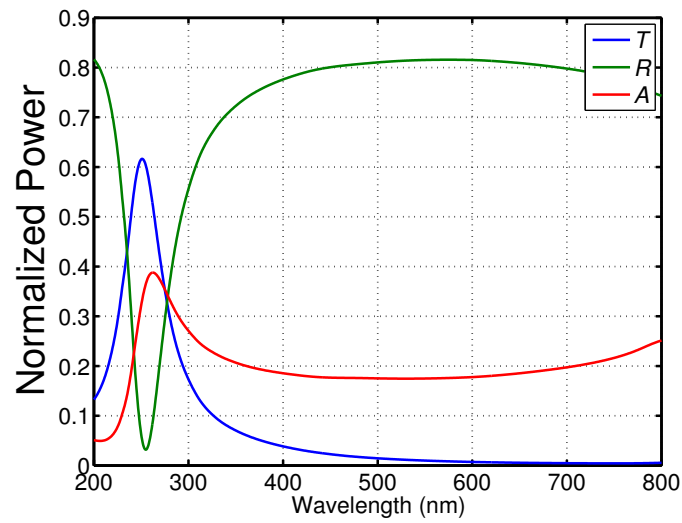
(a) N_p=2
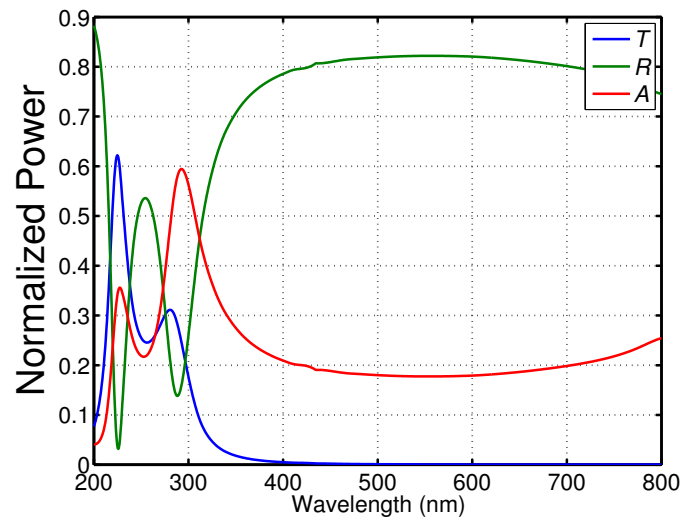
(b) N_p=3

Fig. 3.3. Simulated power spectrum for transmission (T), reflection (R), and absorption (A) for a filter having d_m=10 nm, d_d=50 nm, and θ_{inc}=0° for (a) N_p=2 and (b) N_p=3. Al and SiO$_2$ are used as metal and dielectric, respectively.

Figure 3.3 gives the calculated T, R, and A as a function of wavelength for a UV filter structure with $d_m=10$ nm, $d_d=50$ nm, and with normal illumination ($\theta_{\mathrm{inc}}=0°$); (a) $N_p=2$ and (b) $N_p=3$. Notice that the resonant passband wavelength in Fig. 3.3(a), approximately at 252 nm, is large relative to the dielectric and metal film thicknesses. The phase shift that occurs upon reflection at the dielectric-metal interface allows resonance with small dielectric thickness. This is facilitated by a metal operated close to, yet at wavelengths longer than its plasma frequency (visible wavelength regime for Ag or Au, and UV wavelength regime for Al). In Fig. 3.3(b), with $N_p=3$, two distinct transmission peaks can be observed, compared to a single peak with $N_p=2$ in Fig. 3.3(a). Three unit cells ($N_p=3$) form two coupled cavities, and the modes of these otherwise isolated cavities interact. Consequently, the doubly degenerate single cavity mode splits into two different eigenmodes (252 ± 28 nm) [42]. Here, the longer wavelength peak corresponds to the symmetric mode coupling, and the shorter wavelength peak corresponds to the antisymmetric mode coupling [37]. The magnitude of the resonant transmission peaks differs because of the material (Al) dispersion.

Figure 3.4 shows the spectrum for T (on a logarithmic scale) as a function of illumination angle for transverse electric (TE - E_y, H_x, H_z - Fig. 3.4(a)) and transverse magnetic (TM - H_y, E_x, E_z - Fig. 3.4(b)) cases. The structure dimensions and materials are the same as in Fig. 3.3. For TE, there is moderate sensitivity to incident angle, and for TM, T is essentially independent of angle, except for $\theta_{\mathrm{inc}} \sim 90°$, a regime that is not of practical significance. Filters based on Fabry-Pérot interference with dielectric films typically exhibit substantial sensitivity to angle of incidence, due to changes of phase shift accumulated in the cavity [35]. The metal-dielectric multilayer filter, however, has reduced angular sensitivity for TM.

The angular sensitivity of the filter responses shown in Fig. 3.4 are further analyzed by calculations of phase shift for both TE and TM polarizations, as functions of the incident angle, θ_{inc}, of a single Al-SiO$_2$-Al resonant cavity at $\lambda_0 = 225$ nm. The total round-trip phase shift is $\phi_{\mathrm{tot}} = 2\phi_{\mathrm{ref}} + \phi_{\mathrm{prop}}$ (lines with the circle symbol), where $2\phi_{\mathrm{ref}}$
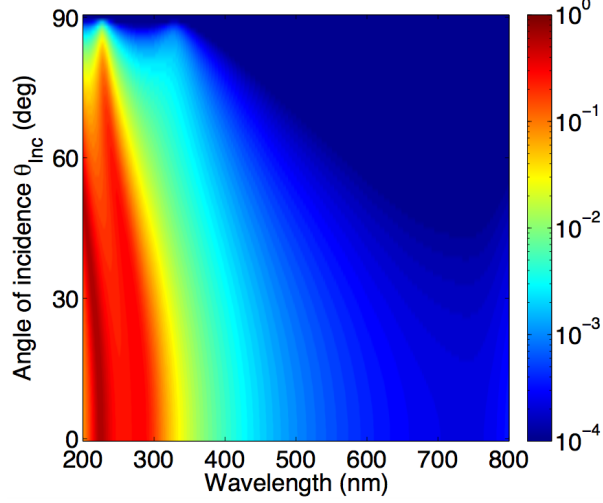
(a) $T(\lambda_0,\theta_{\mathrm{inc}})$, TE
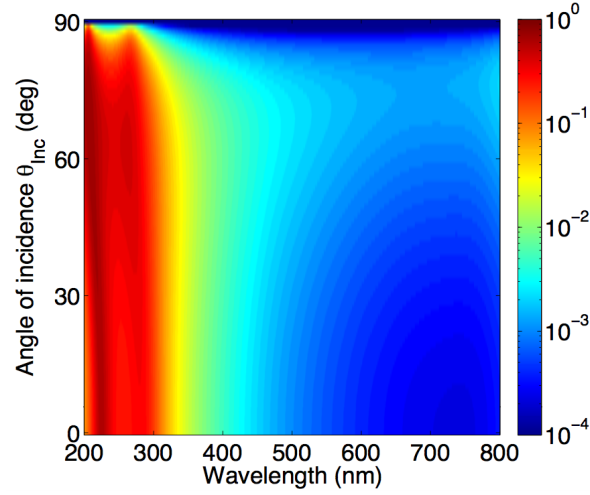
(b) $T(\lambda_0,\theta_{\mathrm{inc}})$, TM

Fig. 3.4. Transmission (T) power spectrum (logarithmic scale) as a function of angle of incidence θ_{inc} for (a) TE and (b) TM illumination. Al and SiO$_2$ are used as metal and dielectric, respectively. The metal thickness d_m=10 nm, the dielectric thickness d_d=50 nm, and the number of periods, N_p=3.

is the reflection phase shift at both cavity walls (dashed lines) and $\phi_{\mathrm{prop}} = 2k_z d_d$ is

the round-trip phase accumulation by wave propagation (blue line). The TE and TM
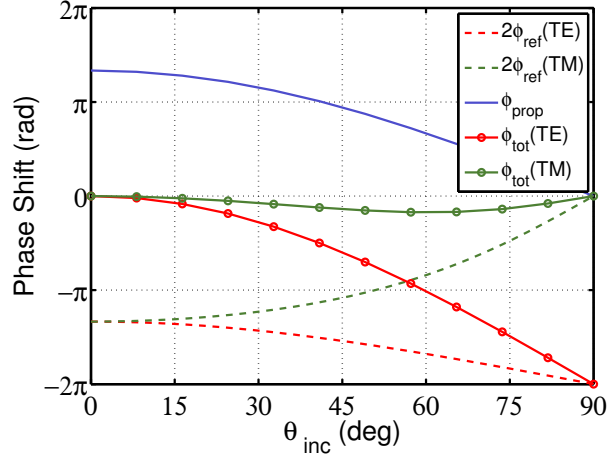
(a) $T(\lambda_0, \theta_{inc})$, TE
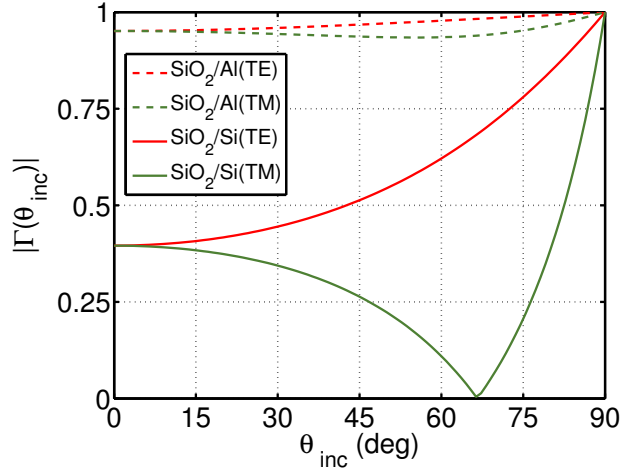
(b) $T(\lambda_0, \theta_{inc})$, TM

Fig. 3.5. (a) The round-trip phase shifts, as a function of incident angle θ_{inc}, of a single Al-SiO$_2$-Al resonant cavity at $\lambda_0 = 225$ nm: the reflection phase shift $2\phi_{ref}$ for TE (red dashed lines) and TM (green dashed lines), the phase accumulation by wave propagation ϕ_{prop} (blue line), and the total phase shift ϕ_{tot} for TE (red line with circles) and TM (green line with circles). (b) Magnitude of the electric field reflection coefficient $|\Gamma(\theta_{inc})|$ for both SiO$_2$/Al (dashed lines) and SiO$_2$/Si (solid lines) interfaces, for TE (red) and TM (green) polarizations.

cases are red and green, respectively. Notice that the trends in angular dependency of $2\phi_{\text{ref}}$ under TE and TM (dashed lines) are opposite. Under TM incidence, $2\phi_{\text{ref}}$ (green dashed line) has the opposite angular dependence compared to ϕ_{prop} (blue line); as a result, the ϕ_{tot} for TM polarized light (line with green circles) is relatively insensitive to angle, and the condition for resonant transmission is approximately satisfied at almost all angles of incidence. Such phase compensation is the underlying principle for the angle-insensitive filter response for TM incidence [39]. Under TE incidence, on the other hand, $2\phi_{\text{ref}}$ (red dashed line) exhibits the same angle-dependence trend as ϕ_{prop}; the resultant ϕ_{tot} (red line with circles) ranges from 0 to -2π as the θ_{inc} goes from $0°$ to $90°$. Nevertheless, as shown in Fig. 3.4(a), the filter response for TE is reasonably insensitive to the angle of incidence for a large range of incident angles ($< 60°$). In Fig. C.1(b), we plot the magnitude of the reflection coefficient $|\Gamma(\theta_{\text{inc}})|$ at a SiO_2/Al (dashed lines) and SiO_2/Si (solid lines) interface for TE (red) and TM (green) polarizations. Notice that $|\Gamma(\theta_{\text{inc}})|$ for the SiO_2/Al case shows remarkably less angle-sensitivity, compared to SiO_2/Si, for both TE and TM cases.

The central resonant wavelength of the transmission passband can be tuned by changing the dielectric thickness. Figure 3.6 shows the T spectrum (logarithmic scale) as a function of dielectric thickness, d_d, with two different numbers of unit cells; (a) $N_p = 3$ and (b) $N_p = 8$. The materials and metal thickness, d_m, are same as in Fig. 3.4, and the illumination is normal ($\theta_{\text{inc}}=0°$). As the dielectric thickness increases, the cavity length increases as well, shifting the resonance to longer wavelengths. The magnitude of the transmission power also varies, showing higher transmission peaks for the UV regime; this is because Al has a lower loss at these wavelengths. Higher order resonant modes begin to appear for larger dielectric thickness. Increasing the number of unit cells leads to additional coupling between the Fabry-Pérot resonators, and as a result, each mode splits into multiple peaks and ripples appear in the pass-band, as shown in Fig. 3.6(b). Also, Fig. 3.6(b) shows a higher wavelength selectivity compared to Fig. 3.6(a), as expected from a higher order filter [35]. As the number of unit cells, N_p, increases, higher quality factor resonators sharpen the cut-off
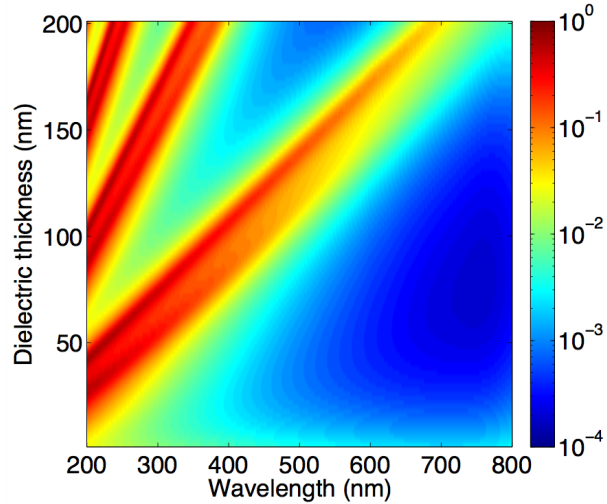
(a) $T(\lambda_0, d_d)$, $N_p=3$
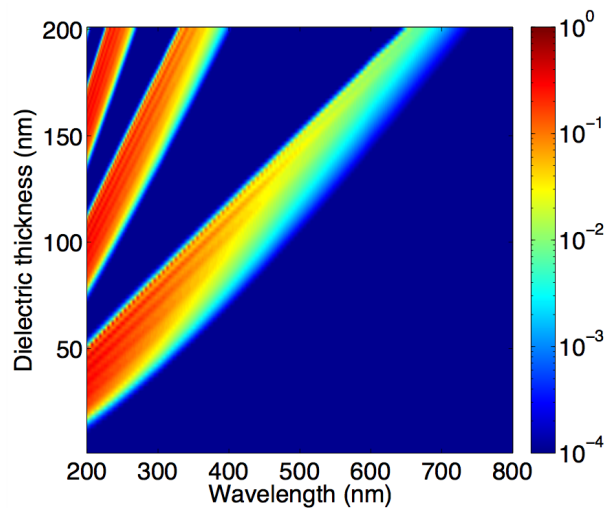
(b) $T(\lambda_0, d_d)$, $N_p=8$

Fig. 3.6. Transmission (T) power spectrum (logarithmic scale) as a function of dielectric thickness d_d when (a) $N_p=3$ and (b) $N_p=8$. Al and SiO$_2$ are used as metal and dielectric, respectively. The metal thickness is $d_m=10$ nm and the illumination is normal ($\theta_{\text{inc}}=0°$).

and introduce passband ripple. This higher wavelength selectivity would improve the sensitivity of a solar-blind UV detector or sensor.

3.4   Conclusion

In conclusion, the metal-dielectric multilayer filter we presented is relatively thin and effective as a solar-blind UV bandpass filter, with angular insensitivity and a high wavelength selectivity. The principle of the metal-insulator stack bandpass filter is not limited for UV applications. By using Ag or Au as the metal whose plasma frequencies fall within the visible or longer wavelength regime, it is possible to design an angle-insensitive filter for visible or longer wavelengths. The reflection phase shift map that we presented can be used to choose appropriate materials. A higher reflection phase shift increases the effective cavity length and provides an angular insensitivity in the filter response. In addition to changing materials, the central wavelength of the transmission band can be easily tuned by the dielectric thickness. This type of angle-insensitive metal-dielectric multilayer filter should be useful in color displays, for optical detectors, and for various spectral analysis that can benefit from insensitivity to the angle of incidence.

4. THE QUEST FOR HOMOGENIZED MAGNETIC MEDIUM

4.1 Introduction

Magnetic effects form the basis of much of modern technology. From data storage to magnetic resonance imaging (MRI), magnetic material responses have been of critical importance. At optical frequencies, however, the magnetic response of natural materials is negligible [43], and the magnetic field couples to atoms much more weakly than does the electric field [44]. As a result, the permeability approaches unity at optical frequencies, and there is no role in controlling the propagation of light. However, during the past decade, research in nanophotonics and plasmonics has demonstrated a range of applications that depend on suitable magnetic material properties at high frequencies, such as high resolution imaging [45], enhanced nonlinearities [46,47], improved MRI resolution [48–51], and magnon waves [52], the dual of surface plasmons. Interest in artificial magnetic media that enable new control of the behavior of light has grown tremendously with the growth of interest in metamaterials [53–57].

Achieving a magnetic metamaterial response requires the excitation of significant magnetic dipole moments in the structure. Such strong interactions between the electromagnetic wave and the material require the underlying structure to produce strong optical scattering, which could occur with a resonance effect. A major emphasis has stemmed from the microwave split-ring resonator (SRR) [46]. This concept of driving circulating current into resonance has since appeared in metamaterial designs that show magnetic response at microwave and terahertz frequencies, and has led to a number of experimental demonstrations of negative refraction [58]. It has also been shown that conduction current in carbon nanotube coil mixtures can provide significant magnetic properties well into the infrared wavelength range [59]. All of this

work has involved conductor concepts and hence is based on the premise of moving free charge. However, at optical frequencies, and by way of example, the material response of noble metals is dominated by displacement current, and the complex dielectric constant has a negative real part [60].

Efforts to increase the operating frequency of SRRs into the optical regime have remained unsuccessful [6], primarily because there is too little free charge and it cannot be moved quickly enough, an argument attributed to Landau and Lifshitz [43]. Several designs have since been reported [61–66] in which resonant surface plasmon modes – displacement current – supported by plamonic nanostructures replaces conduction current in the SRRs. Among these plasmonic metamaterials, the so-called fishnet structure garnered substantial interest [62–64], with reports of negative refractive index in the optical regime [63, 67]. Subsequent work addressed the spatial dispersion that results in strong angular dependence of the retrieved effective medium parameters, challenging a homogenized material picture [68–70]. Another approach that has been presented is use of an array of metal nanoparticles, such as in a ring [6, 65, 66, 71, 71–73] or cluster [74, 75]. A circular ring of such plasmonic particles coupled together can support a circulating displacement current, giving rise to a magnetic dipolar response [65]. While homogenization of such nanoparticles has been investigated (see, for example, [71,73,74]), there remains the question of whether this mode is adequately excited in a mixture and whether substantial magnetism is possible with angle-insensitive homogenization.

While metal nanoparticles provide a strong scatter and a substantial electric dipole moment, they may not be the best choice for achieving a large magnetic dipole. In addition, the non-radiative loss, described by the imaging part of the complex dielectric constant, can be substantial. In some situations, even small losses can severely compromise performance [76, 77]. All-dielectric metamaterials, those with constituent materials having a positive real part of their dielectric constant, may provide an effective suite of properties and low dissipative loss [7, 9, 78–80]. Of key importance here, the series solution of Mie for scatter from a spherical dielectric

particle dictates that the lowest order, longest wavelength resonance is of magnetic dipole character [7–10, 78]. Increasing the dielectric contrast increases the strength of scatter and hence the magnetic dipole moment [9]. Non-spherical dielectric resonators, such as a cube [7, 8], exhibit similar magnetic dipole character.

The excitation of strong magnetic dipole moment in a dielectric particle at optical frequencies can form the microscopic origin of magnetism [7]. However, realizing a homogenized magnetic material response requires a permeability that is insensitive to angle. In a periodic structure, significant scatter occurs at the edges of the Brillouin zone where the lattice dimension (Λ) in an integer multiple of half the effective wavelength (λ). Meaningful homogenization requires frequencies sufficiently far removed from the edge of the Brillouin zone. Forming an intra-cell resonance, as in the magnetic dipole resonance from a dielectric particle, can fulfill this requirement. Because the magnetic dipole resonance on individual particles forms the microscopic origin for optical magnetism, the resonance in the metamaterial relevant to achieving meaningful homogenized permeability μ_{eff} should remain sub-unit-cell in nature, which precludes strong modification of the magnetic dipole resonance as the particles are assembled into a lattice. With weakly interacting scatterers, the resonance frequency for the magnetic dipole of an isolated particle thus sets an upper bound on the size of the lattice, if meaningful homogenization is to be pursued.

We address basic questions of the homogenized magnetic response in relation to the constituent particle's scattering properties and the lattice. For simplicity, we limit our analysis to homogeneous spherical dielectric particles as constituent resonators in the metamaterial, allowing the use of Mie theory for the isolated scatterers to act as a guide. Prior work has considered homogenized magnetism based on the magnetic dipole moment from a Mie-type resonance of the constituent particles [7–9, 78]. Our focus here is the establishment of a correlation between the Mie resonance and the rigorously extracted effective permeability, and how the extracted parameters vary with the key parameters, including frequency, lattice, angle of incidence, and component material properties. The character of scatter from an isolated spherical

particle, the leading electric and magnetic dipole terms in a spherical wavefunction expansion, and the importance of a dielectric particle in achieving a magnetic material response are outlined in Sect. 4.2. Section 4.3 has our key simulation results that show the validity of a homogenized dielectric lattice in realizing a magnetic material response. Section 4.4 presents basic and applied material response issues and the potential impact of the work is summarized in Sect. 4.5.

4.2 Magnetic dipole moment from an isolated particle

We present the calculated scattering efficiency spectrum of a nanometer-scale sphere made of a hypothetical material having dispersionless dielectric constant of 41.7, which corresponds to that of $LiNbO_3$ at terahertz frequencies. This provides a basis for homogenized magnetism and a means to design materials. Specifically, the use of Mie theory facilitates the characterization of the magnetic dipole moment strength arising from a spherical dielectric particle. The exact wave function describing scatter of a linearly-polarized monochromatic plane wave by a homogeneous spherical particle was developed by Mie [10]. The two lowest order terms of the series correspond, respectively, to the fields radiated by a magnetic dipole and an electric dipole. Higher order multipoles occupy corresponding terms of increasing orders in the series expansion. The strength of scatter is characterized by the scattering cross section,

$$\sigma_{\text{sca}} = \frac{\text{Re}\left[\oint_s (\mathbf{E}_{\text{sca}} \times \mathbf{H}_{\text{sca}}^*) \cdot \mathbf{n} \, ds\right]}{\left|\mathbf{E}_{\text{inc}} \times \mathbf{H}_{\text{inc}}^*\right|}. \tag{4.1}$$

A dimensionless quantity, the scattering efficiency, is defined by normalizing σ_{sca} to the geometrical cross section of the particle, giving

$$Q_{\text{sca}} = \frac{\sigma_{\text{sca}}}{\pi a^2}, \tag{4.2}$$

where a is the radius of the spherical particle.

In the series solutions of the scattered field, let a_l and b_l denote the complex amplitude of the l-th electric and magnetic multipole, respectively. These scattering amplitudes have solutions [11]

$$a_l = \frac{n\psi_l'(q)\psi(nq) - \psi_l(q)\psi_l'(nq)}{n\xi_l'(q)\psi_l(nq) - \psi_l'(nq)\xi_l(q)} \tag{4.3}$$

$$b_l = \frac{n\psi_l'(nq)\psi_l(q) - \psi_l(nq)\psi_l'(q)}{n\psi_l'(nq)\xi_l(q) - \psi_l(nq)\xi_l'(q)}, \tag{4.4}$$

where $q = 2\pi a/\lambda$ is the size parameter,

$$\psi_l(z) = \sqrt{\frac{\pi z}{2}}\, J_{l+1/2}(z) \tag{4.5}$$

and

$$\xi_l(z) = \sqrt{\frac{\pi z}{2}}\, H^{(1)}_{l+1/2}(z), \tag{4.6}$$

are the Ricatti-Bessel functions, with $J_\nu(z)$ the Bessel function of the first kind and $H^{(1)}_\nu(z) = J_\nu(z) + iN_\nu(z)$ is the Hankel function of the first kind describing scattered fields, where $N_\nu(z)$ is the Neumann function.

The scattering efficiency Q_{sca} can then be expressed as [11]

$$Q_{\text{sca}} = \frac{2}{q^2} \sum_{l=1}^{\infty} (2l+1)\left(|a_l|^2 + |b_l|^2\right). \tag{4.7}$$

The absorption and extinction efficiencies are determined like wise, with

$$Q_{\text{ext}} = \frac{2}{q^2} \sum_{l=1}^{\infty} (2l+1)\,\text{Re}(a_l + b_l) \tag{4.8}$$

and

$$Q_{\text{abs}} = Q_{\text{ext}} - Q_{\text{sca}}. \tag{4.9}$$

Equation (4.7) is particularly convenient for identifying resonances in the magnetic dipole moment, i.e., local maxima in b_1. As an example, in Fig. 4.1(a) we show the calculated Q_{sca} for an $\epsilon = 41.7$ sphere of radius $a = 80$ nm. The relative contributions from the first three modes are shown, along with the magnetic dipole resonance at $\lambda = 1.05\ \mu$m.
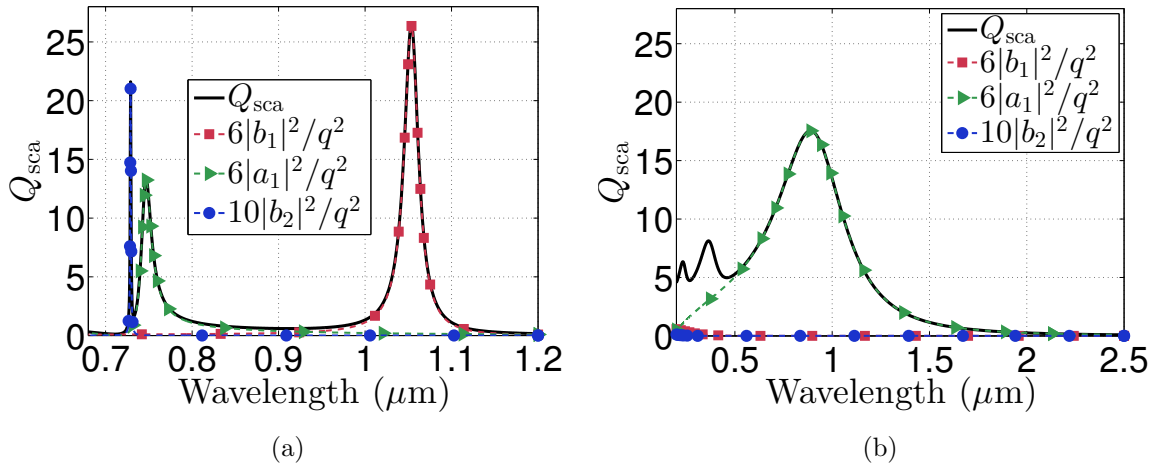
Fig. 4.1. (a) The spectrum of Q_{sca}, and the relative contribution of the first three modes. The dielectric sphere has $\epsilon = 41.7$ radius $a = 80$ nm, and is situated in free space. From the figure the resonance frequencies of magnetic dipole (b_1), electric dipole (a_1), and magnetic quadrapole (b_2) can be determined. Higher order partial waves $(l \geq 3)$ have negligible amplitude at these wavelengths. (b) The case for metal nanoparticle: $a = 160$ nm and $\epsilon = -3$.

For a particle at the reference coordinate center, and an incident plane wave field in the z-direction having $\mathbf{E} = \hat{\mathbf{x}}E_0$, the far-field electric field in spherical coordinates becomes [11]

$$E_\theta^{(s)} \approx E_0 \frac{e^{ikr}}{-ikr} \cos\phi\, S_2(\cos\theta)$$

$$-E_\phi^{(s)} \approx E_0 \frac{e^{ikr}}{-ikr} \sin\phi\, S_1(\cos\theta), \tag{4.10}$$

where η_0 is the free space wave impedance, and S_1 and S_2 are scattering functions represented as an infinite series in terms of Legendre polynomials of order corresponding to the term in the series. The normalized θ-dependent fields, described in (4.10), are plotted in Fig. 4.2 for wavelengths that can be identified as resonances in Fig. 4.1(a). The magnetic and electric dipolar and quadrapolar characters are clear. The magnetic dipole in Fig. 4.2(a) is $\mathbf{m} = \hat{\mathbf{y}}m$ and the electric dipole in Fig. 4.2(b) is $\mathbf{p} = \hat{\mathbf{x}}p$. We exploit the magnetic dipole resonance in creating a homogenized magnetic material.

The magnetic dipole resonance in Fig. 4.1(a), presented in terms of Mie's wave function expansion, can also be viewed in terms of the particle cavity field resonance. A spherical cavity with a perfect electric conductor (PEC) boundary condition has the $\mathrm{TM}_{m,1,1}$ (transverse magnetic to the radial direction, so $H_r = 0$) mode as the lowest order resonance [89]. The internal field for this mode has the form of a electric dipole. The boundary condition at the surface of a large dielectric constant material is approximately at perfect magnetic conductor (PMC). Solving the dual problem for cavity modes results in the lowest order mode being $\mathrm{TE}_{m,1,1}$ and a magnetic dipole character for the internal and scattered fields. Therefore, the enhanced magnetic dipole effect in Fig. 4.1(a) corresponds to the cavity mode of the dielectric particle. Achieving a strong homogenized magnetic material thus corresponds to an intra-cell resonance, as is the case with prior SRR and also that on carbon nanotube (CNT) coil mixtures [59].

In Fig. 4.3 we show the calculated lowest order magnetic dipole resonant wavelength (λ_{md}) as a function of spherical particle radius. Notice that there is linear dependence on particle radius. Also, as expected, the larger the dielectric constant

(a) $\lambda = 1.05$ μm

(b) $\lambda = 0.747$ μm

(c) $\lambda = 0.729$ μm

(d) $\lambda = 0.571$ μm
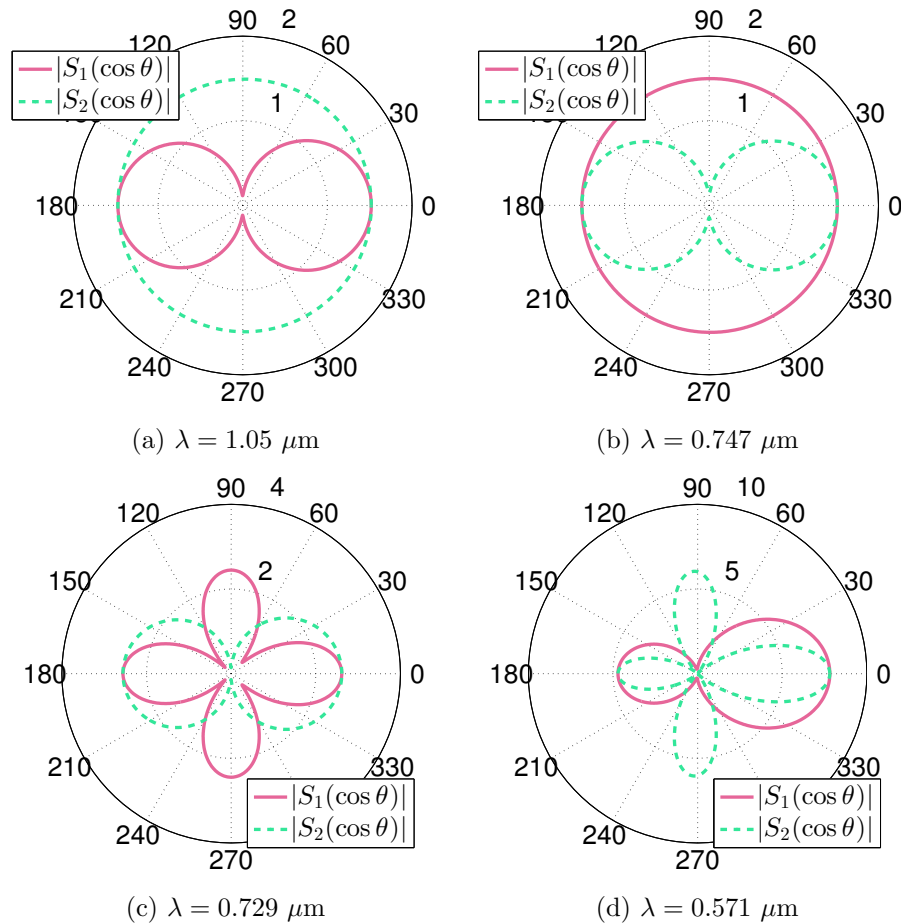
Fig. 4.2. Far-field scattering patterns from (4.10) for an isolated dielectric sphere having $\epsilon = 41.7$ and radius $a = 80$ nm in free space at wavelengths corresponding to resonance in the: (a) magnetic dipole; (b) electric dipole; (c) magnetic quadrapole; (d) electric quadrapole. The resonant wavelengths can be identified in Fig. 4.1(a). The asymmetry in (c) results from multi-pole superposition.
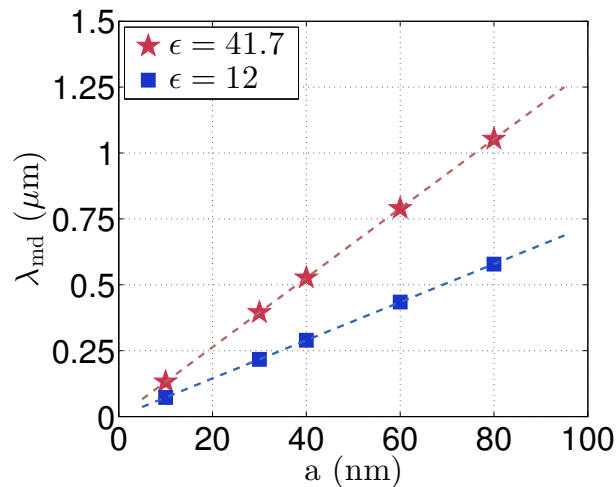
Fig. 4.3. The wavelength for magnetic dipole resonance, λ_{md}, for a dielectric sphere having dielectric constants $\epsilon = 41.7$ (red star symbols, with the red dashed line giving the interpolated results) and $\epsilon = 12$ (blue square symbols and blue dashed line). It is clear that for fixed material, λ_{md} for the dielectric sphere scales linearly with respect to sphere radius over the range of particle radii relevant to this investigation.

that longer the resonant wavelength. In this case, the lower dielectric constant is approximately that for Si. The ratio between the slopes of the two curves is approximately $\sqrt{41.7/12}$.

We point out that the while a dielectric sphere has the magnetic dipole as its dominant and lowest order mode, exhibiting appreciable electric and magnetic multipole resonances, a metal (plasmonic) sphere exhibits almost exclusively the electric multipole resonances with the electric dipole being dominant. While this appears to have been recognized [90,91], in the broader context of desirable material properties, we consider a fictitious, lossless, metal particle in Fig. 4.1(b). Notice that the electric dipole resonance is strong and lowest order, and the magnetic dipole is negligible. This character lead to the conclusion that dielectric spherical nanoparticles (having positive real part of dielectric constant) are the preferred choice over metallic (plasmonic, with a negative real part of the dielectric constant), although both can lead to strong scatter. However, this position may depend on structure, because CNT

coil mixtures that have conduction current resonance have been shown to be a viable magnetic metamaterial [59].

4.3 Homogenized magnetism from dielectric lattices

In this section, we present results for the homogenized material response of dielectric lattices. We first describe a numerical homogenization procedure where we use a finite element method to determine the complex scattered fields at each frequency, hence the S-parameters, and then extract what we claim are the unique material constitutive parameters using a procedure now know as the NRW method [92]. By investigating convergence issues and sensitivity to angle of incidence, we build a case that dielectric spheres on a cubic lattice can provide legitimate homogenized magnetism and exploit the intra-cell magnetic dipole resonance of the isolated particle in Sect. 4.2. We compare this numerical procedure with an analytic method that capture quite nicely the magnetic dipole resonance, providing a simple design framework. Finally, we show results for a candidate optical dielectric material, MoS_2.

4.3.1 Illustrative Homogenized Magnetism from a Dielectric Lattice

We apply the NRW numerical homogenization procedure to the fictitious high dielectric constant material identified as having a suitable magnetic dipole moment in Sect. 4.2, $\epsilon = 41.7$ (LN at THz frequencies) and a spherical radius of $a = 80$ nm. The wavelength λ_{md} corresponding to the magnetic dipole resonance sets an upper bound for the lattice constant Λ, namely $\Lambda < \lambda_{\mathrm{md}}/2$. Clearly, the radius a of the particle sets a lower bound, $2a \leq \Lambda$. Thus, with a given dielectric material, Mie theory can be used to choose a particle size a that yields magnetic dipole resonance in the desired wavelength regime. Then the range of the lattice constant Λ of the metamaterial is conveniently determined from

$$2a < \Lambda < \frac{\lambda_{\mathrm{md}}}{2}. \tag{4.11}$$

We chose a lattice constant of $\Lambda = 280$ nm. Since $\lambda_{md} = 1.05$ μm given the material and $a = 80$ nm, the necessary condition in (4.11) is fulfilled.

The homogenized parameters for this slab is shown in Fig. 4.4. The results for n in Fig. 4.4(a) indicate a passive material at all wavelengths ($n'' > 0$). Although the material is composed of lossless dielectric spheres, there is scattering loss the produces a non-zero n'' in the neighborhood of the intra-cell resonances. In the regime of useful homogenization, there is only one propagating wave scattered from the lattice, that in the normal direction. However, the total near-field solution, including all coefficients of the evanescent plane wave spectrum, influence the complex amplitude of the propagating mode, inducing this apparent loss in the refractive index. The real part of the refractive index can have any sign in principle, but here $n' > 0$. The extracted ($\eta = \sqrt{\mu/\epsilon}$) is shown in Fig. 4.4(b). The real part of the impedance (η') is restricted to be positive, representing positive power flow. The imaginary part of the impedance is unrestricted. Both n and η are uniquely determined from the selection of Γ and z in Step 1. We found that significant homogenized magnetism exists for this structure, as indicated in Fig. 4.4(c), where μ' deviates appreciably from unity at around the wavelength $\lambda = 1.1$ μm. This is near the wavelength ($\lambda_{md} = 1.05$ μm) of the magnetic dipole resonance of an isolated sphere predicted by Mie theory calculations, shown in Fig. 4.1(a). The magnetic resonance is thus of sub-unit-cell nature and occurs at wavelength longer than the edge of the Brillouin zone ($\lambda = 2\Lambda$), and is indicative of valid homogenization. The extracted ϵ is given in Fig. 4.4(d). Notice that the signs of μ'' and ϵ'' change in Figs. 4.4(c) and (d). Those are uniquely determined and collectively provide a passive, slightly lossy medium through n. We return to this issue in Sect. 4.4.

We established convergence in the homogenized parameters as a function of the number of periods in the slab. Figure 4.5 shows a comparison between 1 and 5 units cells, and essentially identical results. While an asymmetric unit cell may require some number of periods to arrive at parameter convergence, depending on the constituent materials, a symmetric unit cell has been shown to have the same extracted
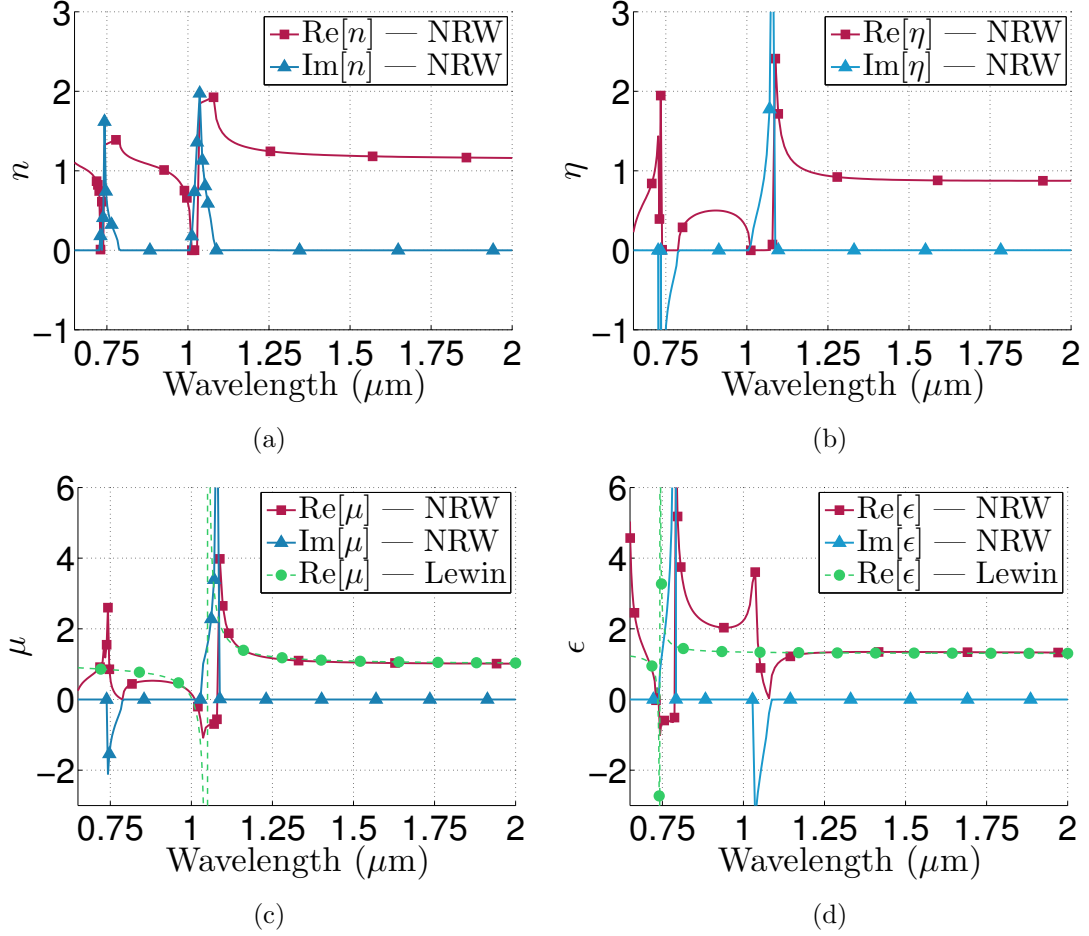
Fig. 4.4. Extracted (a) complex refractive index and (b) $\eta = \sqrt{\mu/\epsilon}$ for a single lattice period with spheres having radius $a = 80$ nm and $\epsilon = 41.7$. The lattice has dimension $\Lambda = 280$ nm and normal incidence is considered. (c) Effective permeability μ and (d) effective permittivity ϵ of a one-unit-cell thick slab. The solid lines correspond to the NRW method and the dashed line the analytical method of Lewin. The magnetic dipole resonance of a single sphere occurs at $\lambda = 1.05$ μm, while the electric dipole resonance occurs at 0.747 μm.
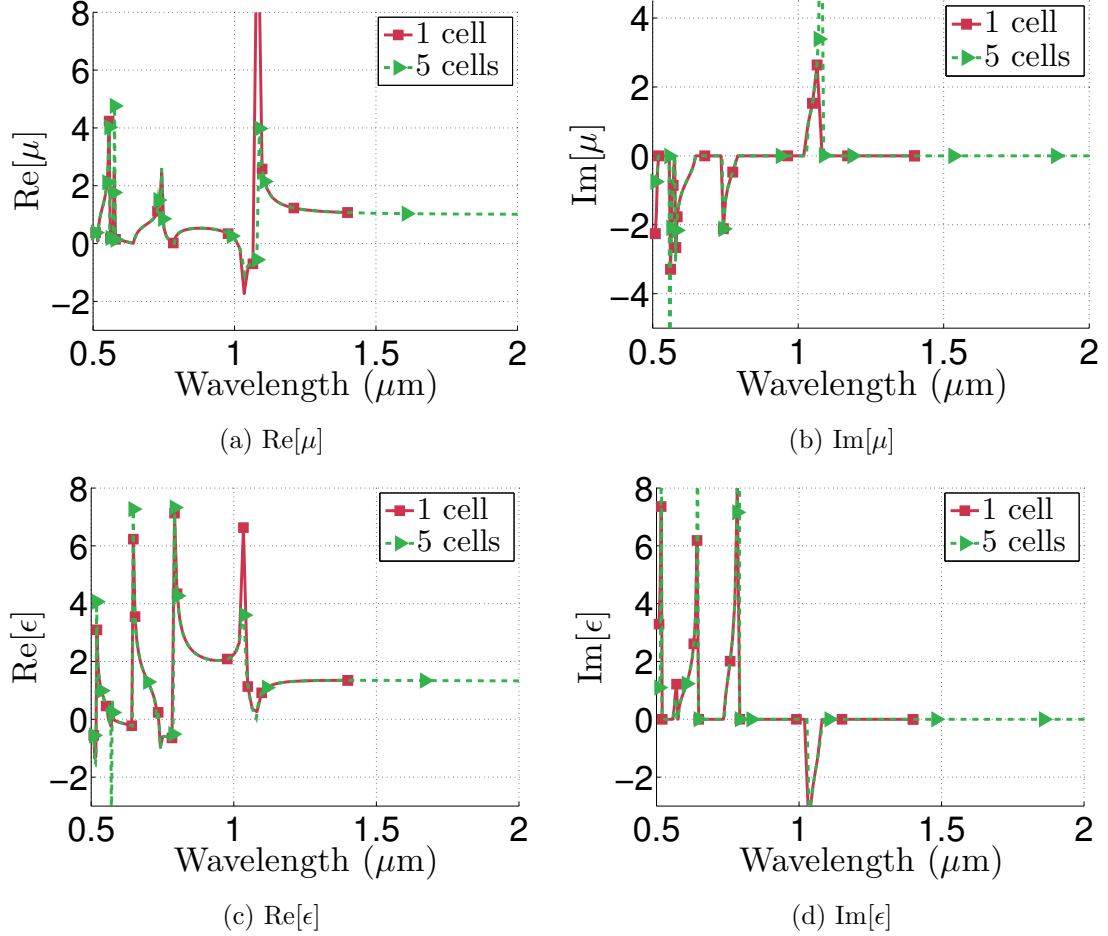
Fig. 4.5. The effective medium properties retrieved using NRW method for stabs measuring one and five unit cells in thickness. The results are virtually identical, indicating one cell is sufficient in our study.

parameters regardless of the number of periods [87]. This along with our numerical data indicates a slab on unit slab thick provides accurate homogenized parameters. For computational expediency, the remainder of our results are for this case.

Valid homogenization should not exhibit dependence on the angle of incidence under which the S-parameters are obtained. Therefore, it is of interest to investigate the angle-dependence of the retrieved effective medium properties. We limit our investigation to TE polarized incidence (electric field perpendicular to the plane defined by the slab surface unit normal vector and the incident wave vector). In Fig. 4.6,

the retrieved effective permeability and permittivity for five angles of incidence are shown. The effective medium properties are found to be largely independent from the angle of incidence up to 30°, but μ' and ϵ' show substantial deviation at 40°, for much of the wavelengths range. Of particular importance is the fact that there is little change μ' at the first resonance as a function of incidence angle. We attribute this to excitation of the dielectric sphere resonance, and it is good news with respect to attaining insensitivity to incidence angle (over the small wavelength range of interest) where there is a substantial homogenized permeability. Our interpretation of these results is that we have shown a legitimately homogenized magnetic material, in this case at $\lambda = 1.05$ μm.

4.3.2 Analytic Homogenization

Lewin developed an analytical procedure for homogenizing a semi-infinite simple cubic lattice loaded with identical dielectric spheres [95]. The problem treated is an infinite homogeneous medium into which scatterers are introduced onto a cubic lattice in a semi-infinite half-space. This conforms with our situation of dielectric spheres arranged to this point in a slab and in free space. We apply this method of homogenization and compare with the numerical NRW approach with a slab.

In Lewin's work, the reflected and transmitted fields are expressed as a sum of the scattered fields of the particles in the lattice. This uses Mie theory but retains only the first two terms in the partial wave expansion. Weakly interacting scatterers are assumed, which means either low fill fraction or small dielectric constant scatterers. The constitutive parameters of the effective medium, ϵ and μ, are extracted following the determination of reflection and transmission coefficients at the boundary of the semi-infinite effective medium [95]. In this aspect it is similar to the NRW method. We provide the results from Lewin here because they a plotted in comparison with

(a) Re[μ]

(b) Im[μ]

(c) Re[ϵ]

(d) Im[ϵ]
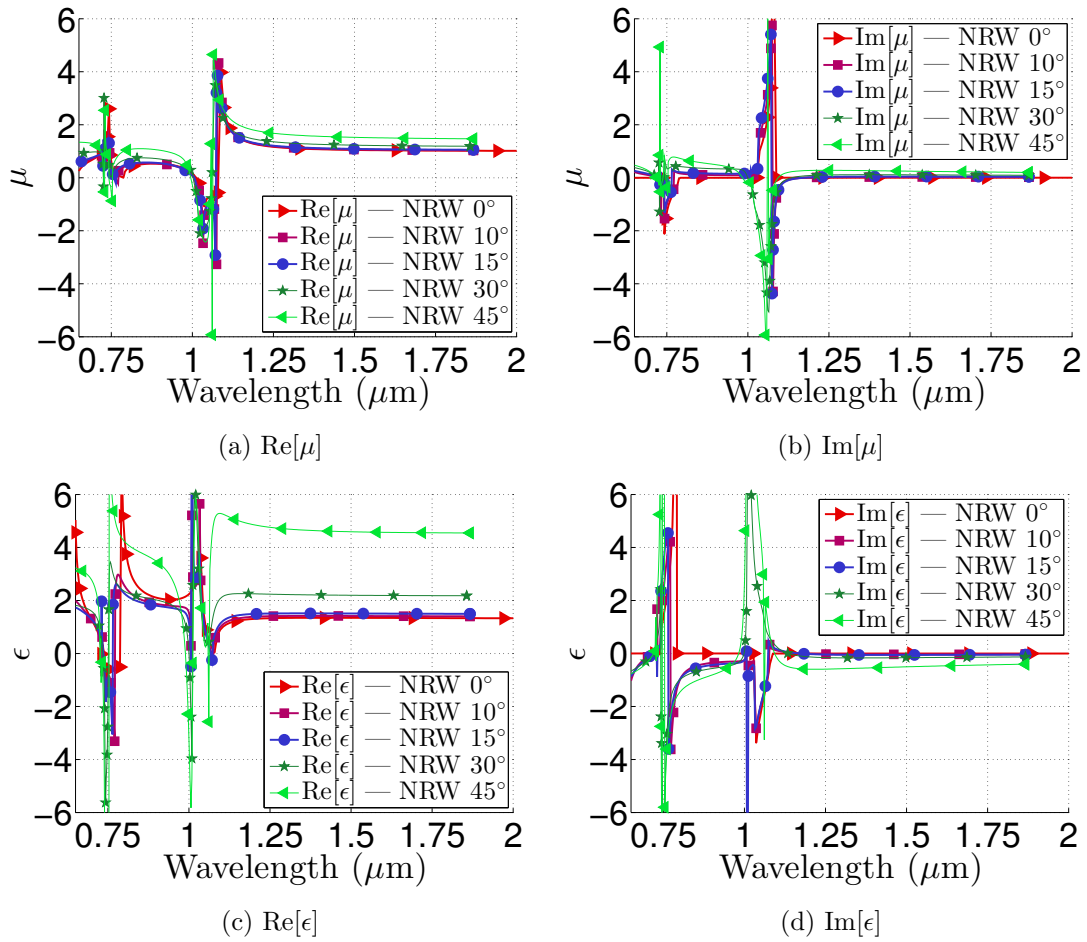
Fig. 4.6. The homogenization results for a structure with dielectric $\epsilon = 41.7$ spheres 80 nm in radius on a simple cubic lattice with Lattice constant $\Lambda = 280$ nm as a function of incident angle. The finite slab is 1 unit cell thick.

our numerical slab results and the fact that they can provide a design framework. The homogenized parameters [95],

$$\epsilon = \epsilon_1 \left(1 + \frac{3v_f}{\frac{F(\theta)+2b_e}{F(\theta)-b_e} - v_f} \right) \tag{4.12}$$

$$\mu = \mu_1 \left(1 + \frac{3v_f}{\frac{F(\theta)+2b_m}{F(\theta)-b_m} - v_f} \right), \tag{4.13}$$

where

$$F(\theta) = \frac{2(\sin\theta - \theta\cos\theta)}{(\theta^2 - 1)\sin\theta + \theta\cos\theta}, \tag{4.14}$$

ϵ_1 and μ_1 are the dielectric constant and the relative permeability of the background medium, respectively, and ϵ_2 and μ_2 are those of the particle,

$$b_e = \frac{\epsilon_1}{\epsilon_2}, \qquad b_m = \frac{\mu_1}{\mu_2}, \tag{4.15}$$

the volume filling fraction is

$$v_f = \frac{4\pi}{3} \left(\frac{a}{\Lambda} \right)^3, \tag{4.16}$$

and

$$\theta = \left(\frac{\omega}{c} \right) a\sqrt{\epsilon_2\mu_2}. \tag{4.17}$$

For the lattice under consideration, $\epsilon_1 = 1$, $\epsilon_2 = 41.7$, and $\mu_1 = \mu_2 = 1$. The homogenized effective medium parameters are shown in Figs. 4.4(c) and (d) for comparison with the numerical results for a slab with NRW extraction. The Lewin parameters are real, as dissipative losses are absent in the constituent particles. The resonances in μ and ϵ occurs at wavelengths that corresponds respectively to the magnetic dipole resonance at $\lambda = 1.05$ μm and the electric dipole resonance at $\lambda = 0.747$ μm of an isolated sphere, shown in Fig. 4.2(a) and (b). Notice how nicely μ' is captured through the magnetic dipole resonance in the mixture in Fig. 4.4(c), the major feature of interest here, and how the electric dipole resonance is captured in Fig. 4.4(d). In the analytical results, ϵ is not affected by resonance in the magnetic dipole. Similarly, the μ is not affected by resonance in the electric dipole. In the numerical results obtained using the NRW method, any multipole resonance affects both the electric

and magnetic homogenized responses. For wavelengths longer than that of magnetic dipole resonance (λ_{md}), the two methods agree perfectly. Although Lewin uses expansion terms up to quadrapole, the results are in agreement with the more accurate numerical procedure only through the dipole resonances. We attribute this deviation to the strength of scatter this medium.

4.3.3 Magnetism from Patterned Transition Metal Dichalcogenides

Among naturally existing materials, TMDs possess large positive dielectric constant over a wide spectrum range. The striking relevant feature of TMDs is their large sheet dielectric constant and low loss in the near-infrared [97]. This suggests a strong magnetic dipole moment at a Mie resonance. Based on the bulk MoS_2 dielectric constant [96], we approximate the dielectric constant as being isotropic and use the values in Fig. 4.7(a). The calculated optical scattering spectrum for an MoS_2 sphere 80 nm in radius is shown in Fig. 4.7(b). It is evident from the scattering spectrum that an appreciable magnetic dipole resonance occurs at incident wavelength 0.79 μm. We subsequently homogenize a structure consisting of MoS_2 spheres with 80 nm radius on a simple cubic unit lattice with lattice constant $\Lambda = 280$ nm using the numerical NRW procedure, and find the retrieved effective medium properties are shown in Figs. 4.7(c) and (d) for the normal incidence case. We found that significant homogenized magnetic response exists for this structure, as indicated in Fig. 4.7(c) near the wavelength of magnetic dipole resonance of an isolated MoS_2 sphere predicted by Mie theory calculations, shown in Fig. 4.7(b). The magnetic resonance is thus again of sub-unit-cell nature and occurs at wavelength longer than the edge of the Brillouin zone ($\lambda = 2\Lambda$), the two necessary conditions for legitimate homogenization. We show the results from Lewin's homogenization, and it again does a remarkable job through the magnetic and electric dipole resonances, capturing the complex constitutive parameters.

4.4   Discussion

4.4.1   Uniqueness and Extraction of Homogenized Material Properties

Section 4.3 presented a a numerical procedure to determine the homogenized parameters of a slab of known thickness using the NRW approach. While fitting a parameterized model to a data set is an optimization problem, with complex S-parameters at each frequency, the NRW procedure is convenient. Our FEM simulations played the role of experimental data. At microwave and even THz frequencies, phase information (including though time domain data) is routinely obtained. At optical frequencies, phase information can be obtained with an interferometer measurement (see [98] for example), and this is now routinely achieved done in obtaining the transmission matrix [99]. However, it is most common and convenient to measure intensities at optical frequencies, as in ellipsometry. Material properties can be determined from such experimental data with a forward model, and some of our earlier work presents an example approach for single stacked 2D materials [100].

We described a procedure in Sect. 4.3 whereby the material parameters can be uniquely determined. This requires S-parameter data at sufficiently low frequencies so that the phase progression over the thickness of the slab is less than 2π. If this cannot be realized, then there is a uniqueness problem in the selection of k, within modulo 2π. However, by using multiple incident angles at each frequency, it is in principle possible to circumvent this problem and obtain the unique material parameters. Furthermore, in an experiment, varying sample thicknesses may be possible, further aided unique extraction of the material properties.

4.4.2   Constitutive Parameters

The cubic lattice symmetry means that the homogenized material is isotropic, and that μ and ϵ should describe the material response. This will of course only be possible with angle-independent material parameters when homogenization is legitimate. We made the case that this was true through the isolated particle magnetic dipole

resonance in the mixtures we considered, and in particular, over wide angles at that resonance. This provides a basis for realizing an optical magnetic material.

The basis for potential optical magnetism is weak spatial dispersion of second order, as has been extensively presented (see, for example, [59, 87, 101]). Consequently, the basis is the spatially varying material, providing a non-local in space (as well as time) material-field relationship. Therefore, as the lattice shrinks and the material contrast diminishes, spatial dispersion reduces and so will homogenized μ. The challenge faced in realizing a homogenized optical magnetic material then becomes one of a sufficiently strongly scattering material with an adequately small lattice size, relative to the wavelength, to allow homogenization. In addition, there are aspects of the material properties and the spatial arrangement of materials within the unit cell that impact μ. We have shown that dielectric rather than metal ($\epsilon' > 0$ rather than $\epsilon' < 0$) is important. at least for spherical inclusions. However, the game is to pack a intra-cell resonant material into the unit cell in a way that allows homogenization and a substantial scattering cross-section at resonance and a large magnetic dipole (per unit volume).

Our procedure involved the extraction of k and η, and then ϵ and μ. All of these parameters become unique with enforcement of passivity (for k and n) and then the determination of unique ϵ and μ as secondary and fundamental parameters, as far as Maxwell's equations are concerned. The extraction procedure enforced passivity, and hence all results at all wavelengths (whether or not homogenization is meaningful) are for a lossy material that will produce field decay with increase in propagation distance ($k'' > 0$ and $n'' > 0$ for $\exp(-i\omega t)$). Passive material properties reflected in complex μ and ϵ usually have $\mu'' > 0$ and $\epsilon'' > 0$. Notice that both μ'' and ϵ'' change signs around resonances in Figs. 4.4, 4.6 and 4.7, but of course $k'' > 0$. There is no freedom of sign choice in the NRW homogenization, so the precise signs of the complex μ and ϵ are predetermined. We considered this issue extensively, both is terms of uniqueness and sign choice, and the legitimacy of homogenization. We find that homogenization is appropriate over substantial angular ranges at the magnetic dipole resonance, and

that there can be situations where one of the constitutive parameters reflect gain when the overall material is lossy, and that this extraction is unique. There is substantial treatment in the literature of anti-resonance, where one of the constituent materials exhibits gain [56]. There has been concern that this is a violation of causality and that it occurs when homogenization fails [93, 102]. We find neither to be the case in the situations of primary interest here and around the magnetic dipole resonance.

So-called Bloch materials that display an anti-resonance [103]. The response of such materials has been found to exist with increasing number of periods. In this sense, the responses we have presented would appear to be Bloch materials. However, we should emphasize that the homogenized material descriptions presented match the numerical field calculations at all wavelengths, and that over a large wavelength range that spans through the first magnetic dipole resonance, a homogenized description predicts the numerical results. We have thus found a regime where homogenization is valid while simultaneously fitting within this Bloch lattice framework.

4.4.3   Causality

We return to causality because it is fundamental and because anti-resonance has been associated with violation of causality. Anecdotally, we solve Maxwell's equations for the lattice to numerical precision, so subject to this precision, causality is implied because of the mathematical basis of the representation. The homogenized material description agrees with the numerical result, including where an anti-resonance occurs (but the material remains passive). Therefore, we have anecdotal evidence that causality is upheld and that an anti-resonance does not preclude this. Of course, a system with gain can also be causal. What has led to the concern about anti-resonance is the local (anomalous dispersion) shape of the material parameter as a function of frequency (μ' or ϵ' in the neighborhood of an anti-resonance). The wave packet group velocity ($v_g = d\omega/dk'$) is approximate, itself non-causal (because of the truncated spectral representation) and known to have anomalies in the neighborhood

of resonances. This is immaterial because the exact time domain field solution can be constructed from a temporal Fourier transform description.

The Kramers-Kronig relations [104], which result from causality, are given by the Hilbert transform pair

$$
\begin{aligned}
\zeta'(\omega) - 1 &= \frac{2}{\pi} \fint_0^\infty \frac{\omega' \zeta''(\omega')}{\omega'^2 - \omega^2} d\omega' \\
\zeta''(\omega) &= \frac{-2\omega}{\pi} \fint_0^\infty \frac{\zeta'(\omega') - 1}{\omega'^2 - \omega^2} d\omega',
\end{aligned}
\tag{4.18}
$$

where $\zeta = \zeta' + i\zeta''$ and $\zeta \in \{\mu, \epsilon, n^2\}$, the reality of $\zeta(t)$ has been enforced, and the integral is interpreted as a principal value, with the pole residue evaluated. The mathematical basis of (4.18) is an integral theorem [105] that uses Cauchy's integral theorem. The physical basis is that the local atomic excitation by the wave cannot occur at a time prior to this distance divided by the speed of light in vacuum, which forms the local $t = 0$ condition used in deriving (4.18). Of relevance here is the fact that (4.18) does not place any specific requirement on the local dispersive properties of the material, only in the integral sense. For example, gain and anti-resonance are not strictly forbidden, although of course one could construct solutions with these characteristics that do not satisfy (4.18). Our homogenized results, by virtue of the solution method, will satisfy (4.18). One may view ζ a a response function that satisfies $\zeta(t) = 0$ for local time $t < 0$. Because we treat a homogenized material with local electric and magnetic dipole moments, $n = \sqrt{\mu\epsilon}$. we can thus apply (4.18) to n or k. In either case, our homogenized material responses are passive and hence must satisfy (4.18). Thus, collectively (n) and separately (ϵ and μ), the homogenized material properties we have extracted satisfy causality requirements.

4.4.4   Prospects for Optical Magnetism

We have established that a lattice of dielectric spheres can lead to homogenized magnetism. The fact that $\epsilon' > 0$ leads to low-loss opportunities for creating optical magnetic materials have substantial μ. The requirement for large a ϵ' material could be met by TMDs, perhaps in a layered arrangement, and Si. We note that prior work

on Si resonators showed the prospects for magnetic effects [7]. Our work went further by addressing the homogenized material issues. The requirement of a large dielectric constant material is one of achieving a magnetic dipole resonance within the unit cell. At conditions away from this resonance, there may still be useful μ, but the difference from unity will diminish.

Negative index lenses have been proposed for achieving high resolution. A true negative index requires $\mu' < 0$ and $\epsilon' < 0$. The major challenge has been achieving $\mu' < 0$ - metals for instance provide $\epsilon' < 0$. Our results in Figs. 4.4, 4.6 and 4.7 indicate that μ' can be negative. However, the density of the material should be high relative to the relevant wavelength [106]. Evanescent fields have a high transverse spatial frequency, and the lattice dimension we considered will not satisfy this requirement. However, recent work on negative index lens properties [57] suggests it may be possible to exploit a different material regime that may be accessible based on work presented here.

Based on our work, non-spherical dielectrics such as patterned Si on a lower dielectric material might provide a viable optical magnetic material for applications. By using a silicon-on-insulator (SOI) substrate, developed for electronic devices, the top Si layer could be patterned and the contrast would exist with the woer index SiO_2 layer. Also, the exfoliated and tarnsfer of TMD materials onto a quartz substrate, as we did for graphene stack materials [100], may also provide a path for implementation. The homogenization of Lewin provides a simple start for designs, and refinements could use numerical modeling, as we did.

4.5   Conclusions

We have shown that dielectric metamaterials provide a viable low-loss means to achieve a homogenized opical magnetic material. The microscopic origin of their homogenized magnetic response derives from magnetic dipole resonance of the individual constituent particles. We have demonstrated that with high-index materials, such a magnetic dipole resonance could occur at frequencies in the optical regime.

In the case of spherical particle inclusions, Mie theory becomes a valuable analytical method in the determination of the resonance frequency the magnetic dipole mode, and its dependence on material properties and particle size. The more complicated cases of arbitrarily-shaped particle of heterogeneous composition, e.g., core-shell, can be considered as a perturbation from the homogeneous spherical case. For particles of less regular shapes or compositions, numerical modeling would be needed and the scattering properties would become polarization-dependent. The validity of homogenized effective medium properties is justified based on their lack of variation with respect to the angle of incidence, particularly in the neighborhood of the magnetic dipole resonance. The use of naturally existing high-index materials as constituents is also considered. For instance, transition metal dichalcogenides are shown to be effective in building resonators with substantial magnetic dipole resonance.
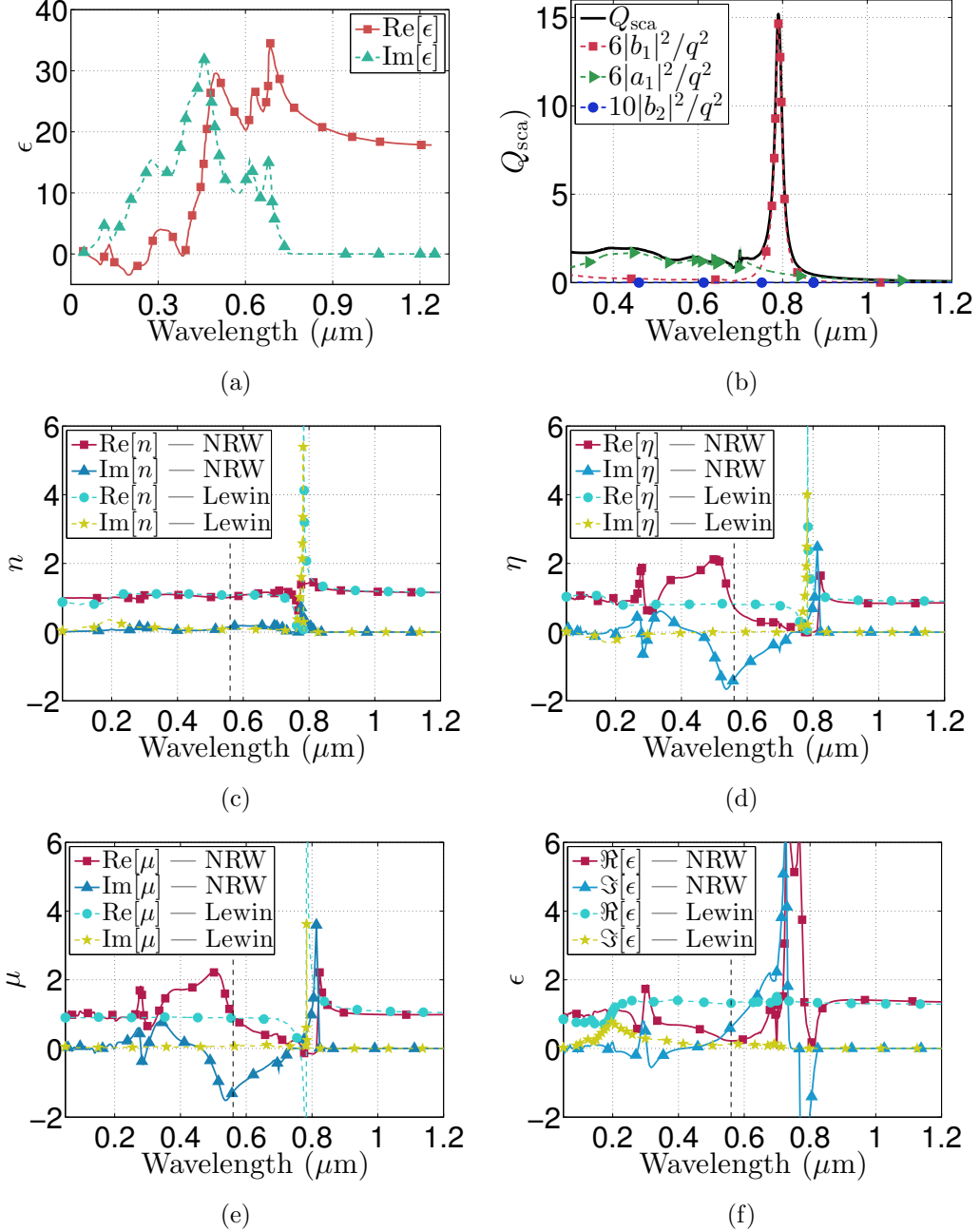
Fig. 4.7. (a) The dielectric constant of MoS_2 plotted as a function of the wavelength of light [96]. For $\lambda > 0.7$ μm the material is almost lossless, suitable for applications in homogenized magnetism. (b) Scattering efficiency from a Mie expansion for an 80 nm radius MoS_2 sphere. Note the strong magnetic dipole resonance at 0.79 μm. Homogenized (c) n and (d) $\eta = \sqrt{\mu/\epsilon}$ for a one unit cell thick lattice of spherical particles on a simple cubic grid: $\Lambda = 280$ nm. The MoS_2 spheres have radius $a = 80$ nm. The strong resonance in μ at 0.79 μm corresponds to the magnetic dipole resonance in (b). The edge of the first Brillouin zone corresponds to a free-space wavelength $\lambda = 0.56$ μm.

5. SUMMARY

The thesis presented three topics in nanophotonics research for application as light-absorbing dark materials, bandpass filters, and magnetic metamaterials. The main accomplishments of these research activities are summarized below.

1. In Chapter 2, we demonstrated the design of an efficient light-absorbing dark material using a stack of graphene and dielectric. Its effectiveness was verified with experiments involving ellipsometric measurement of graphene conductance, fabrication of graphene/dielectric stacks, and characterization of optical reflection and transmission. A new model for analyzing data from ellipsometry measurements was developed, which took into account the 2D nature of graphene and the incoherent superposition of light due to reflection from the back of transparent quartz substrate. This ellipsometry data analysis procedure could be useful in studying other 2D materials such as chalcogenides.

2. In Chapter 3, the concept of a bandpass filter that shows little sensitivity to the angle of incidence was demonstrated. The filter is based on a metal/dielectric stack structure, similar to the graphene stack. The insensitivity to angle of incidence derives from the nontrivial phase shift at the interface between metal and dielectric, whose angular dependence tends to cancel that of the phase shift arising from propagation within the dielectric layer. The filter pass band is a result of resonant transmission of the coupled Fabry-Pèrot cavities formed by alternating layers of metal and dielectric. Aluminum was identified as the material of choice for retaining metallic character at UV frequencies due to its high plasma frequency. Filter passbands can be shifted to the visible or longer wavelength by adjusting thickness of dielectric layers and choosing materials with suitable plasma frequency.

3. Chapter 4 presents a detailed study of dielectric metamaterials consisting of spherical resonators arranged on a simple cubic lattice. We consider a hypothetical material having permittivity $\epsilon = 41.7$, corresponding to that of $LiNbO_3$ at terahertz frequencies. The absence of metallic or plasmonic components allows the metamaterial to be free of resistive losses that prohibits useful optical applications. Using Mie theory, the resonance frequency for the magnetic dipole moment of a spherical particle is calculated. It was found that features in the homogenized effective permeability correspond in frequency to the magnetic dipole resonance of individual spherical particle. The results establish explicitly that the magnetic dipole resonances of the individual resonators in a metamaterial lie at the microscopic origin of homogenized magnetic response. In the case of spherical particle inclusions, Mie theory becomes a valuable aid in identifying the frequencies of the magnetic dipole resonance and its dependence on material properties and particle size. For legitimate homogenization, the magnetic dipole resonance should correspond to a wave number well within the first Brillouin zone. Hence, for a given material and sphere radius, one can conveniently obtain an upper bound on the lattice constant using only Mie theory calculations. The more complicated cases involving dielectric particles of arbitrary shapes can be guided with preliminary studies based on spherical particles made of the same materials.

REFERENCES

REFERENCES

[1] K. F. Mak, M. Y. Sfeir, Y. Wu, C. H. Lui, J. A. Misewich, and T. F. Heinz, "Measurement of the optical conductivity of graphene," *Phys. Rev. Lett.*, vol. 101, p. 196405, Nov 2008.

[2] M. Razeghi, "Short-wavelength solar-blind detectors-status, prospects, and markets," *Proc. IEEE*, vol. 90, no. 6, pp. 1006–1014, 2002.

[3] R. Safin, I. Gaǐnutdinov, R. Sabirov, and M. K. Azamatov, "Solar-blind filter for the ultraviolet region," *J. Opt. Technol.*, vol. 74, no. 3, pp. 208–210, 2007.

[4] W.-D. Li and S. Y. Chou, "Solar-blind deep-uv band-pass filter (250-350 nm) consisting of a metal nano-grid fabricated by nanoimprint lithography," *Opt. Express*, vol. 18, no. 2, pp. 931–937, 2010.

[5] E. D. Palik, *Handbook of Optical Constants of Solids.* Academic press, 1998, vol. 3.

[6] J. Zhou, T. Koschny, M. Kafesaki, E. N. Economou, J. B. Pendry, and C. M. Soukoulis, "Saturation of the magnetic response of split-ring resonators at optical frequencies," *Phys. Rev. Lett.*, vol. 95, p. 223902, 2005.

[7] J. C. Ginn, I. Brener, D. W. Peters, J. R. Wendt, J. O. Stevens, P. F. Hines, L. I. Basilio, L. K. Warne, J. F. Ihlefeld, P. G. Clem, and M. B. Sinclair, "Realizing optical magnetism from dielectric metamaterials," *Phys. Rev. Lett.*, vol. 108, no. 9, p. 097402, 2012.

[8] L. K. Warne, L. I. Basilio, W. L. Langston, W. A. Johnson, and M. B. Sinclair, "Perturbation theory in the design of degenerate rectangular dielectric resonators," *Prog. Electromagn. Res. B*, vol. 44, pp. 1–29, 2012.

[9] A. I. Kuznetsov, A. E. Miroshnichenko, Y. H. Fu, J. Zhang, and B. Luk'yanchuk, "Magnetic light," *Sci. Rep.*, vol. 2, 2012.

[10] G. Mie, "Beiträge zur optik trüber medien, speziell kolloidaler metallösungen," *Annalen der Physik*, vol. 330, no. 3, pp. 377–445, 1908.

[11] C. F. Bohren and D. R. Huffman, *Absorption and Scattering of Light by Small Particles.* John Wiley & Sons, 1983.

[12] M. Born and E. Wolf, *Principles of Optics.* Cambridge University Press, 1999.

[13] L. Britnell, R. Ribeiro, A. Eckmann, R. Jalil, B. Belle, A. Mishchenko, Y.-J. Kim, R. Gorbachev, T. Georgiou, S. Morozov *et al.*, "Strong light-matter interactions in heterostructures of atomically thin films," *Science*, vol. 340, no. 6138, pp. 1311–1314, 2013.

[14] H. M. Branz, V. E. Yost, S. Ward, K. M. Jones, B. To, and P. Stradins, "Nanostructured black silicon and the optical reflectance of graded-density surfaces," *Appl. Phys. Lett.*, vol. 94, no. 23, pp. 231 121 –231 121–3, jun 2009.

[15] R. Brown, M. Milton *et al.*, "The physical and chemical properties of electroless nickel–phosphorus alloys and low reflectance nickel–phosphorus black surfaces," *J. of Mater. Chem.*, vol. 12, no. 9, pp. 2749–2754, 2002.

[16] Z. Yang, L. Ci, A. James, S. Lin, and P. Ajayan, "Experimental observation of an extremely dark material made by a low-density nanotube array," *Nano Lett.*, vol. 8, no. 2, pp. 446–451, 2008.

[17] A. Ludwig and K. Webb, "Dark materials based on graphene sheet stacks," *Opt. Lett.*, vol. 36, no. 2, pp. 106–108, 2011.

[18] C. Lee, J. Kim, S. Bae, K. Kim, B. Hong, and E. Choi, "Optical response of large scale single layer graphene," *Appl. Phys. Lett.*, vol. 98, no. 7, pp. 071 905–071 905, 2011.

[19] H. Yan, X. Li, B. Chandra, G. Tulevski, Y. Wu, M. Freitag, W. Zhu, P. Avouris, and F. Xia, "Tunable infrared plasmonic devices using graphene/insulator stacks," *Nature Nanotech.*, vol. 7, no. 5, pp. 330–334, 2012.

[20] K. V. Sreekanth, S. Zeng, J. Shang, K.-T. Yong, and T. Yu, "Excitation of surface electromagnetic waves in graphene-based Bragg grating," *Sci. Rep.*, vol. 2, p. Art. 737, 2012.

[21] A. Reina, X. Jia, J. Ho, D. Nezich, H. Son, V. Bulovic, M. S. Dresselhaus, and J. Kong, "Large area, few-layer graphene films on arbitrary substrates by chemical vapor deposition," *Nano Lett.*, vol. 9, no. 1, pp. 30–35, 2008.

[22] X. Li, W. Cai, J. An, S. Kim, J. Nah, D. Yang, R. Piner, A. Velamakanni, I. Jung, E. Tutuc *et al.*, "Large-area synthesis of high-quality and uniform graphene films on copper foils," *Science*, vol. 324, no. 5932, pp. 1312–1314, 2009.

[23] R. Joerger, K. Forcht, A. Gombert, M. Köhl, and W. Graf, "Influence of incoherent superposition of light on ellipsometric coefficients," *Appl. Opt.*, vol. 36, no. 1, pp. 319–327, 1997.

[24] K. Forcht, A. Gombert, R. Joerger, and M. Köhl, "Incoherent superposition in ellipsometric measurements," *Thin Solid Films*, vol. 302, no. 1, pp. 43–50, 1997.

[25] E. M. Ferreira, M. V. Moutinho, F. Stavale, M. Lucchese, R. B. Capaz, C. Achete, and A. Jorio, "Evolution of the raman spectra from single-, few-, and many-layer graphene with increasing disorder," *Phys. Rev. B*, vol. 82, no. 12, p. 125429, 2010.

[26] C. Casiraghi, S. Pisana, K. Novoselov, A. Geim, and A. Ferrari, "Raman fingerprint of charged impurities in graphene," *Appl. Phys. Lett.*, vol. 91, no. 23, pp. 233 108–233 108, 2007.

[27] T. Ando, Y. Zheng, and H. Suzuura, "Dynamical conductivity and zero-mode anomaly in honeycomb lattices," *J. Phys. Soc. Jp.*, vol. 71, no. 5, pp. 1318–1324, 2002.

[28] A. Kuzmenko, E. Van Heumen, F. Carbone, and D. Van Der Marel, "Universal optical conductance of graphite," *Phys. Rev. Lett.*, vol. 100, no. 11, p. 117401, 2008.

[29] P. Yeh, *Optical Waves in Layered Media.* Wiley, 1988, vol. 95.

[30] S. Bae, H. Kim, Y. Lee, X. Xu, J.-S. Park, Y. Zheng, J. Balakrishnan, T. Lei, H. R. Kim, Y. I. Song *et al.*, "Roll-to-roll production of 30-inch graphene films for transparent electrodes," *Nature Nanotech.*, vol. 5, no. 8, pp. 574–578, 2010.

[31] H. Fujiwara, "Principles of spectroscopic ellipsometry," *Spectroscopic Ellipsometry: Principles and Applications*, 2007.

[32] F. Xia, T. Mueller, R. Golizadeh-Mojarad, M. Freitag, Y.-m. Lin, J. Tsang, V. Perebeinos, and P. Avouris, "Photocurrent imaging and efficient photon detection in a graphene transistor," *Nano Lett.*, vol. 9, no. 3, pp. 1039–1044, 2009.

[33] J. Yan, M. Kim, J. Elle, A. Sushkov, G. Jenkins, H. Milchberg, M. Fuhrer, and H. Drew, "Dual-gated bilayer graphene hot-electron bolometer," *Nature Nanotech.*, vol. 7, no. 7, pp. 472–478, 2012.

[34] Z. Zheng, C. Zhao, S. Lu, Y. Chen, Y. Li, H. Zhang, and S. Wen, "Microwave and optical saturable absorption in graphene," *Opt. Express*, vol. 20, no. 21, pp. 23 201–23 214, 2012.

[35] H. A. Macleod, *Thin Film Optical Filters.* Taylor & Francis, 2001.

[36] M. Scalora, M. Bloemer, A. Pethel, J. Dowling, C. Bowden, and A. Manka, "Transparent, metallo-dielectric, one-dimensional, photonic band-gap structures," *J. Appl. Phys.*, vol. 83, no. 5, pp. 2377–2383, 1998.

[37] M. R. Gadsdon, J. Parsons, and J. R. Sambles, "Electromagnetic resonances of a multilayer metal-dielectric stack," *J. Opt. Soc. Am. B*, vol. 26, no. 4, pp. 734–742, 2009.

[38] H. Liu, Shivanand, and K. J. Webb, "Optical circuits from anisotropic films," *Phys. Rev. B*, vol. 79, no. 9, p. 094 203, 2009.

[39] H. Shin, M. F. Yanik, S. Fan, R. Zia, and M. L. Brongersma, "Omnidirectional resonance in a metal–dielectric–metal geometry," *Appl. Phys. Lett.*, vol. 84, no. 22, pp. 4421–4423, 2004.

[40] J.-L. Zhang, W.-D. Shen, P. Gu, Y.-G. Zhang, H.-T. Jiang, and X. Liu, "Omnidirectional narrow bandpass filter based on metal-dielectric thin films," *Appl. Opt.*, vol. 47, no. 33, pp. 6285–6290, 2008.

[41] A. D. Rakić, "Algorithm for the determination of intrinsic optical constants of metal films: application to aluminum," *Appl. Opt.*, vol. 34, no. 22, pp. 4755–4767, 1995.

[42] Q. Li, T. Wang, Y. Su, M. Yan, and M. Qiu, "Coupled mode theory analysis of mode-splitting in coupled cavity system," *Opt. Express*, vol. 18, no. 8, pp. 8367–8382, 2010.

[43] L. D. Landau and E. M. Lifshitz, *Electrodynamics of Continuous Media.* Oxford, UK: Pergamon, 1960.

[44] A. Alu and N. Engheta, "The quest for magnetic plasmons at optical frequencies," *Opt. Express*, vol. 17, no. 7, pp. 5723–5730, 2009.

[45] J. B. Pendry, "Negative refraction makes a perfect lens," *Phys. Rev. Lett.*, vol. 85, no. 18, p. 3966, 2000.

[46] J. Pendry, A. Holden, D. Robbins, and W. Stewart, "Magnetism from conductors and enhanced nonlinear phenomena," *IEEE Trans. Microw. Theory Techn.*, vol. 47, no. 11, pp. 2075–2084, 1999.

[47] Y. Kobljanskyj, G. Melkov, K. Guslienko, V. Novosad, S. D. Bader, M. Kostylev, and A. Slavin, "Nano-structured magnetic metamaterial with enhanced nonlinear properties," *Sci. Rep.*, vol. 2, 2012.

[48] Y. Xie, J. Jiang, and S. He, "Proposal of cylindrical rolled-up metamaterial lenses for magnetic resonance imaging application and preliminary experimental demonstration," *Prog. Electromagn Res.*, vol. 124, pp. 151–162, 2012.

[49] C. Scarborough, Z. Jiang, D. Werner, C. Rivero-Baleine, and C. Drake, "Experimental demonstration of an isotropic metamaterial super lens with negative unity permeability at 8.5 mhz," *Appl. Phys. Lett.*, vol. 101, no. 1, p. 014101, 2012.

[50] M. J. Freire and R. Marques, "Optimizing the magnetoinductive lens: Improvement, limits, and possible applications," *J. Appl. Phys.*, vol. 103, no. 1, p. 013115, 2008.

[51] J. M. Algarin, M. J. Freire, M. A. Lopez, M. Lapine, P. M. Jakob, V. C. Behr, and R. Marqués, "Analysis of the resolution of split-ring metamaterial lenses with application in parallel magnetic resonance imaging," *Appl. Phys. Lett.*, vol. 98, no. 1, p. 014105, 2011.

[52] G. Dolling, M. Wegener, A. Schädle, S. Burger, and S. Linden, "Observation of magnetization waves in negative-index photonic metamaterials," *Appl. Phys. Lett.*, vol. 89, no. 23, p. 231118, 2006.

[53] D. Smith, S. Schultz, P. Markoš, and C. Soukoulis, "Determination of effective permittivity and permeability of metamaterials from reflection and transmission coefficients," *Phys. Rev. B*, vol. 65, no. 19, p. 195104, 2002.

[54] D. Smith, D. Vier, T. Koschny, and C. Soukoulis, "Electromagnetic parameter retrieval from inhomogeneous metamaterials," *Phys. Rev. E*, vol. 71, no. 3, p. 036617, 2005.

[55] M. Kafesaki, I. Tsiapa, N. Katsarakis, T. Koschny, C. Soukoulis, and E. Economou, "Left-handed metamaterials: The fishnet structure and its variations," *Phys. Rev. B*, vol. 75, no. 23, p. 235114, 2007.

[56] T. Koschny, P. Markoš, D. Smith, and C. Soukoulis, "Resonant and antiresonant frequency dependence of the effective parameters of metamaterials," *Phys. Rev. E*, vol. 68, no. 6, p. 065602, 2003.

[57] Y. Chen, Y.-C. Hsueh, M. Man, and K. J. Webb, "Enhanced and tunable resolution from an imperfect negative refractive index lens," *J. Opt. Soc. Am. B*, vol. 33, no. 3, pp. 445–451, 2016.

[58] D. R. Smith, W. J. Padilla, D. Vier, S. C. Nemat-Nasser, and S. Schultz, "Composite medium with simultaneously negative permeability and permittivity," *Phys. Rev. Lett.*, vol. 84, no. 18, pp. 4184–4187, 2000.

[59] A. Ludwig, K. J. Webb, and H. Ågren, "Magnetism from carbon nanocoil mixtures," *J. Appl. Phys.*, vol. 118, no. 15, p. 153104, 2015.

[60] P. B. Johnson and R.-W. Christy, "Optical constants of the noble metals," *Phys. Rev. B*, vol. 6, no. 12, p. 4370, 1972.

[61] V. A. Podolskiy, A. K. Sarychev, and V. M. Shalaev, "Plasmon modes in metal nanowires and left-handed materials," *J. Nonlinear Opt. Phys. Mater.*, vol. 11, no. 01, pp. 65–74, 2002.

[62] S. Zhang, W. Fan, N. C. Panoiu, K. J. Malloy, R. Osgood, and S. R. J. Brueck, "Experimental demonstration of near-infrared negative index metamaterials," *Phys. Rev. Lett.*, vol. 95, p. 137404, Sep. 2005.

[63] J. Valentine, S. Zhang, T. Zentgraf, E. Ulin-Avila, D. A. Genov, G. Bartal, and X. Zhang, "Three-dimensional optical metamaterial with a negative refractive index," *Nature*, vol. 455, no. 7211, pp. 376–379, 2008.

[64] C. García-Meca, R. Ortuno, F. Rodriguez-Fortuno, J. Martí, and A. Martínez, "Double-negative polarization-independent fishnet metamaterial in the visible spectrum," *Opt. Lett.*, vol. 34, no. 10, pp. 1603–1605, 2009.

[65] F. Shafiei, F. Monticone, K. Q. Le, X.-X. Liu, T. Hartsfield, A. Alù, and X. Li, "A subwavelength plasmonic metamolecule exhibiting magnetic-based optical fano resonance," *Nature Nanotech.*, vol. 8, no. 2, pp. 95–99, 2013.

[66] F. Monticone and A. Alù, "The quest for optical magnetism: from split-ring resonators to plasmonic nanoparticles and nanoclusters," *J. Mater. Chem. C*, 2014.

[67] Z. Wei, Y. Cao, J. Han, C. Wu, Y. Fan, and H. Li, "Broadband negative refraction in stacked fishnet metamaterial," *Appl. Phys. Lett.*, vol. 97, no. 14, p. 141901, 2010.

[68] C. Rockstuhl, C. Menzel, T. Paul, T. Pertsch, and F. Lederer, "Light propagation in a fishnet metamaterial," *Phys. Rev. B*, vol. 78, no. 15, p. 155102, 2008.

[69] C. Menzel, C. Rockstuhl, T. Paul, F. Lederer, and T. Pertsch, "Retrieving effective parameters for metamaterials at oblique incidence," *Phy. Rev. B*, vol. 77, no. 19, p. 195328, 2008.

[70] C. Menzel, T. Paul, C. Rockstuhl, T. Pertsch, S. Tretyakov, and F. Lederer, "Validity of effective material parameters for optical fishnet metamaterials," *Phys. Rev. B*, vol. 81, no. 3, p. 035320, 2010.

[71] A. Alù and N. Engheta, "Dynamical theory of artificial optical magnetism produced by rings of plasmonic nanoparticles," *Phys. Rev. B*, vol. 78, no. 8, p. 085112, 2008.

[72] A. Alù, A. Salandrino, and N. Engheta, "Negative effective permeability and left-handed materials at optical frequencies," *Opt. Express*, vol. 14, no. 4, pp. 1557–1567, 2006.

[73] D. Morits and C. Simovski, "Negative effective permeability at optical frequencies produced by rings of plasmonic dimers," *Phys. Rev. B*, vol. 81, no. 20, p. 205112, 2010.

[74] C. R. Simovski and S. A. Tretyakov, "Model of isotropic resonant magnetism in the visible range based on core-shell clusters," *Phys. Rev. B*, vol. 79, p. 045111, Jan 2009. [Online]. Available: http://link.aps.org/doi/10.1103/PhysRevB.79.045111

[75] D. Morits and C. Simovski, "Isotropic negative effective permeability in the visible range produced by clusters of plasmonic triangular nanoprisms," *Metamaterials*, vol. 5, no. 4, pp. 162–168, 2011.

[76] M.-C. Yang and K. J. Webb, "Poynting vector analysis of a superlens," *Opt. Lett.*, vol. 30, no. 18, pp. 2382–2384, 2005.

[77] Z. Guo, Q. Huang, C. Wang, P. Gao, W. Zhang, Z. Zhao, L. Yan, and X. Luo, "Negative and positive impact of roughness and loss on subwavelength imaging for superlens structures," *Plasmonics*, vol. 9, no. 1, pp. 103–110, 2014.

[78] Q. Zhao, J. Zhou, F. Zhang, and D. Lippens, "Mie resonance-based dielectric metamaterials," *Mater. Today*, vol. 12, no. 12, pp. 60–69, 2009.

[79] S. Jahani and Z. Jacob, "All-dielectric metamaterials," *Nat. Nanotechnol.*, vol. 11, no. 1, pp. 23–36, 2016.

[80] A. Ahmadi and H. Mosallaei, "Physical configuration and performance modeling of all-dielectric metamaterials," *Phys. Rev. B*, vol. 77, no. 4, p. 045104, 2008.

[81] N. W. Ashcroft and N. D. Mermin, *Solid State Physics*. Philadelphia: Saunders, 1976.

[82] J. C. Maxwell Garnett, "Colours in metal glasses and in metallic films," *Philos. Trans. R. Soc. Lond.*, vol. 203, pp. 385–420, 1904.

[83] ——, "Colours in metal glasses, in metallic films, and in metallic solutions. ii," *Philos. Trans. R. Soc. Lond.*, vol. 205, pp. 237–288, 1906.

[84] K. J. Webb and A. Ludwig, "Semiconductor quantum dot mixture as a lossless negative dielectric constant optical material," *Phys. Rev. B*, vol. 78, p. 153303, 2008.

[85] A. Serdyukov, I. Semchenko, S. Tretyakov, and A. Sihvola, *Electromagnetics of Bi-anisotropic Materials: Theory and Applications*, ser. Electrocomponent Science Monographs. Amsterdam: Gordon and Breach Science Publishers, 2001, vol. 11.

[86] A. Sihvola, *Electromagnetic Mixing Formulae and Applications*, ser. Electromagnetic Waves Series.   London: IEE Publishing, 1999, vol. 47.

[87] A. Ludwig and K. J. Webb, "Accuracy of effective medium parameter extraction procedures for optical metamaterials," *Phys. Rev. B*, vol. 81, no. 11, p. 113103, 2010.

[88] D. R. Smith, J. Gollub, J. J. Mock, W. J. Padilla, and D. Schurig, "Calculation and measurement of bianisotropy in a split ring resonator metamaterial," *J. Appl. Phys.*, vol. 100, no. 2, p. 024507, 2006.

[89] R. F. Harrington, *Time-Harmonic Electromagnetic Fields.*   New York: McGraw-Hill, 1961.

[90] M. I. Tribelskii, "Resonant scattering of light by small particles," *Sov. Phys. JETP*, vol. 59, no. 3, pp. 534–536, 1984.

[91] B. S. Luk'yanchuk, M. I. Tribel'skiĭ, and V. Ternovskiĭ, "Light scattering at nanoparticles close to plasmon resonance frequencies," *J. Opt. Technol.*, vol. 73, no. 6, pp. 371–377, 2006.

[92] A. Nicolson and G. Ross, "Measurement of the intrinsic properties of materials by time-domain techniques," *IEEE Trans. Instrum. Meas.*, vol. 19, no. 4, pp. 377–382, 1970.

[93] A. Alù, "First-principles homogenization theory for periodic metamaterials," *Phys. Rev. B*, vol. 84, no. 7, p. 075153, 2011.

[94] C. Simovski, "Material parameters of metamaterials (a review)," *Opt. Spectrosc.*, vol. 107, no. 5, pp. 726–753, 2009.

[95] L. Lewin, "The electrical constants of a material loaded with spherical particles," *J. Inst. Electr. Eng. 3*, vol. 94, no. 27, pp. 65–68, 1947.

[96] A. Beal and H. Hughes, "Kramers-kronig analysis of the reflectivity spectra of $2H\text{-}MoS_2$, $2H\text{-}MoSe_2$ and $2H\text{-}MoTe_2$," *J. Phys. C: Solid State Physics*, vol. 12, no. 5, p. 881, 1979.

[97] Y. Li, A. Chernikov, X. Zhang, A. Rigosi, H. M. Hill, A. M. van der Zande, D. A. Chenet, E.-M. Shih, J. Hone, and T. F. Heinz, "Measurement of the optical dielectric function of monolayer transition-metal dichalcogenides: Mos_2, $mose_2$, ws_2, and wse_2," *Phys. Rev.B*, vol. 90, no. 20, p. 205422, 2014.

[98] M. Webster, T. Gerke, A. Weiner, and K. Webb, "Spectral and temporal speckle field measurements of a random medium," *Opt. Lett.*, vol. 29, no. 13, pp. 1491–1493, 2004.

[99] S. M. Popoff, G. Lerosey, R. Carminati, M. Fink, A. C. Boccara, and S. Gigan, "Measuring the transmission matrix in optics: an approach to the study and control of light propagation in disordered media," *Phys. Rev. Lett.*, vol. 104, no. 10, p. 100601, 2010.

[100] S. Chugh, M. Man, Z. Chen, and K. J. Webb, "Ultra-dark graphene stack metamaterials," *Appl. Phys. Lett.*, vol. 106, no. 6, p. 061102, 2015.

[101] A. Serdyukov, I. Semchenko, S. Tretyakov, and A. Sihvola, *Electromagnetics of Bi-anisotropic Materials: Theory and Applications*. Gordon and Breach, 2001.

[102] A. Alù, "Restoring the physical meaning of metamaterial constitutive parameters," *Phys. Rev. B*, vol. 83, no. 8, p. 081102, 2011.

[103] C. R. Simovski, "Bloch material parameters of megneto-dielectric metamaterials and the concepts of bloch lattices," *Metamaterials*, vol. 1, pp. 62–80, Sep. 2007.

[104] J. D. Jackson, *Classical Electrodynamics*, 3rd ed. New York, NY: Wiley, 1999.

[105] E. C. Titchmarsh, *Introduction to the Theory of Fourier Integrals*. Oxford, UK: Oxford University Press, 1948.

[106] J. Li and K. Webb, "Influence of granularity on the optical properties of a negative-refractive-index lens," *Phys. Rev. A*, vol. 78, no. 1, p. 015803, 2008.

[107] H. Fujiwara, *Spectroscopic Ellipsometry: Principles and Applications*. Wiley Online Library, 2007.

[108] MATLAB, *version 8.1.0.604 (R2013a)*. Natick, Massachusetts: The MathWorks Inc., 2013.

[109] E. Kreyszig, *Advanced Engineering Mathematics*. John Wiley & Sons, 2007.

APPENDICES

A. ELLIPSOMETRY ANALYSIS WITH CONSIDERATION OF INCOHERENT SUPERPOSITION

We provide the ellipsometry analysis method used to extract the wavelength-dependent complex sheet conductivity of graphene. Our contributions here include the derivation of a set of modified Fresnel coefficients that incorporate sheet conductivity at the interface between two media. These new Fresnel coefficients fit our optical model of graphene and enabled us to extract its sheet conductivity by matching a forward model calculation (with spectral averaging) to measured data.

Spectroscopic ellipsometry gives a measures the ratio of the electric field reflection coefficients for TE (r_{TE}) and TM (r_{TM}) components as a function of wavelength [107]. The ellipsometer provides two sets of wavelength-dependent data, Ψ_{exp} and Δ_{exp}, and the ratio is expressed as a function of $r_{\text{TE}}/r_{\text{TM}} = \tan \Psi_{\text{exp}} \exp(i\Delta_{\text{exp}})$. In the extraction procedure, we express these two quantities in terms of an unknown complex sheet conductivity, σ_s, and denote them as $\Psi_{\text{calc}}(\sigma_s)$ and $\Delta_{\text{calc}}(\sigma_s)$. These quantities, as recorded by a power detector in the ellipsometer, are a result of superposition over the detector bandwidth, and the data are impacted with the thick (0.5 mm) quartz substrate used in the experiment. We expressed $\Psi_{\text{calc}}(\sigma_s)$ and $\Delta_{\text{calc}}(\sigma_s)$ in terms of averaged reflectance.

Previous studies have established that Ψ_{exp} and Δ_{exp} can be expressed as functions of reflectances for four distinct polarizations, $R(0°)$, $R(45°)$, $R(90°)$, and $R_\gamma(45°)$, where the angles in the argument refer to orientation of electric field with respect to the plane of incidence [23, 24]. We show the derivation in detail. Consider coherent linearly-polarized incident light. The reflected field with amplitude normalized to that of the incident field is

$$E_x = |r_s| \cos(\tau + \delta_1), \tag{A.1}$$

$$E_y = |r_p| \cos(\tau + \delta_2), \tag{A.2}$$

where

$$\tau = \omega t - \mathbf{k} \cdot \mathbf{r}, \tag{A.3}$$

$$a_1 = |r_s|, \tag{A.4}$$

$$a_2 = |r_p|. \tag{A.5}$$

The relation between these quantities and the ellipsometric angles Ψ and Δ are

$$\Delta = \delta_2 - \delta_1, \tag{A.6}$$

$$\tan \Psi = \frac{a_2}{a_1} = \frac{|r_p|}{|r_s|}, \tag{A.7}$$

$$\tan \Psi \exp(i\Delta) = \frac{r_p}{r_s}. \tag{A.8}$$

Define the intensity reflectance at an arbitrary angle of polarization ϕ as

$$R(\phi) = |E_\xi|^2. \tag{A.9}$$

Note that the amplitude of E_ξ is already normalized to that of incdient light. For definition of the angle ϕ, please refer to Fig. A.1.

From Fig. A.1, one can see that

$$\begin{pmatrix} E_\xi \\ E_\eta \end{pmatrix} = \begin{pmatrix} \cos \phi & \sin \phi \\ -\sin \phi & \cos \phi \end{pmatrix} \begin{pmatrix} E_x \\ E_y \end{pmatrix} \tag{A.10}$$

Hence,

$$\begin{aligned} R(\phi) &= |r_x \cos \phi + r_p \sin \phi|^2 \\ &= r_s r_s^* \cos^2 \phi + r_p r_p^* \sin^2 \phi + (r_s r_p^* + r_s^* r_p) \cos \phi \sin \phi. \end{aligned} \tag{A.11}$$

We can relate $(r_s r_p^* + r_s^* r_p)$ to Δ by writing

$$r_p = |r_p| e^{i\delta_2} \tag{A.12}$$

$$r_s = |r_s| e^{i\delta_1} \tag{A.13}$$

Fig. A.1. The polarization ellipse for the electric field vector of light reflected from graphene sample, which is the locus of the electric field vector $\mathbf{E}(t)$ in a plane normal to the wavevector of reflected plane wave. The smallest circumscribing rectangle is shown in red. The x- and y-axes are determined by the setup of the ellipsometer. The blue rectangle circumscribes the vibrational ellipse and has major axes along x- and y-directions.

$$\Delta = \delta_2 - \delta_1 \tag{A.14}$$

$$\cos\Delta = \frac{r_s r_p^* + r_s^* r_p}{2|r_s r_p^*|} = \frac{r_s r_p^* + r_s^* r_p}{2\sqrt{R_s R_p}}, \tag{A.15}$$

where

$$R_s = |r_s|^2, \qquad R_p = |r_p|^2. \tag{A.16}$$

Hence,

$$2\sqrt{R_s R_p}\cos\Delta = r_s r_p^* + r_s^* r_p. \tag{A.17}$$

Therefore, the power reflectance at arbitrary $\phi \in [0, \pi]$ is

$$R(\phi) = R_s \cos^2\phi + R_p \sin^2\phi + 2\sqrt{R_s R_p}\cos\Delta \cos\phi \sin\phi. \tag{A.18}$$

There are two special cases for linearly polarized light,

$$\text{TM:} \quad \phi = \frac{\pi}{2}, \quad R_p = r_p r_p^* = R(90°) \tag{A.19}$$

$$\text{TE:} \quad \phi = 0, \quad R_s = r_s r_s^* = R(0°) \tag{A.20}$$

With incoherent incident light, we need to average $R(\phi)$ over a certain bandwidth.

We now show that Ψ and Δ can be expressed in terms of the intensity reflectances $R(\phi)$ for $\phi \in \{0°, 45°, 90°, 135°\}$. Define the three parameters,

$$\alpha = \cos 2\Psi \tag{A.21}$$

$$\beta = \sin 2\Psi \cos \Delta \tag{A.22}$$

$$\gamma = \sin 2\Psi \sin \Delta. \tag{A.23}$$

First, write α in terms of R_s and R_p. Since

$$\tan \Psi = \frac{|r_p|}{|r_s|}, \tag{A.24}$$

$$\tan^2 \Psi = \frac{R_p}{R_s}. \tag{A.25}$$

We have

$$\cos^2 \Psi = \frac{1}{1 + \tan^2 \Psi} = \frac{R_s}{R_s + R_p} \tag{A.26}$$

Hence,

$$\alpha = \cos 2\Psi = 2\cos^2 \Psi - 1 = \frac{R_s - R_p}{R_s + R_p}. \tag{A.27}$$

In the above equation, the power reflectances R_s and R_p can be readily averaged over the spectral range of interest to take into account the incoherent superposition of light due to an optically thick and transparent substrate. Similarly for β,

$$\beta = \sin 2\Psi \cos \Delta = \sqrt{1 - \alpha^2} \cos \Delta = \frac{2\sqrt{R_s R_p}}{R_s + R_p} \cos \Delta. \tag{A.28}$$

From Eq. (A.15), we can write β as

$$\beta = \frac{2\sqrt{R_s R_p}}{R_s + R_p} \cdot \frac{r_s r_p^* + r_s^* r_p}{2\sqrt{R_s R_p}} = \frac{r_s r_p^* + r_s^* r_p}{R_s + R_p}. \tag{A.29}$$

For $\phi = 45°$, we have

$$
\begin{aligned}
R(45°) &= R(0°)\cos^2 45° + R(90°)\sin^2 45° + (r_s r_p^* + r_s^* r_p)\cos 45° \sin 45° \\
&= \frac{1}{2}\left[R(0°) + R(90°) + r_s r_p^* + r_s^* r_p\right]
\end{aligned} \tag{A.30}
$$

Hence,

$$
r_s r_p^* + r_s^* r_p = 2R(45°) - R(0°) - R(90°). \tag{A.31}
$$

Therefore,

$$
\beta = \frac{2R(45°)}{R(0°) + R(90°)} - 1. \tag{A.32}
$$

This leads to

$$
2\sqrt{R_s R_p}\cos\Delta = 2\operatorname{Re}[r_s r_p^*] \tag{A.33}
$$

$$
R(0°) = R_s = \langle r_s r_s^* \rangle \tag{A.34}
$$

$$
R(90°) = R_p = \langle r_p r_p^* \rangle \tag{A.35}
$$

$$
R(45°) = R_s \cos^2 45° + R_p \sin^2 45° + 2\operatorname{Re}\left[\langle r_s r_p^* \rangle\right]\sin\phi\cos\phi \tag{A.36}
$$

Spectral averaging was carried out for these reflectances. Given the optical thickness of the substrate, the phase difference accumulated by traversing the substrate, between frequency components at the two ends of the detector bandwidth, is significantly larger than 2π. It is therefore valid and convenient to derive analytical expressions for spectrally averaged reflectances by evaluating

$$
\langle R(\alpha) \rangle = \frac{1}{2\pi}\int_0^{2\pi} R(\alpha)\, \mathrm{d}\delta_n, \tag{A.37}
$$

where δ_n is the phase accumulated in traversing the substrate, $R(\alpha)$ is the power reflectance with the electric field making an angle α with the plane of incidence, and $\langle\cdot\rangle$ is the average.

For our sample with two interfaces, where the top is air-graphene-quartz and the bottom is quartz-air, the electric field reflection coefficient is [12]

$$
r = \frac{r_{12} + r_{23}e^{i2\delta_n}}{1 + r_{12}r_{23}e^{i2\delta_n}}, \tag{A.38}
$$

leading to the intensity reflectance

$$R = |r|^2. \tag{A.39}$$

where r_{12} is the electric field reflection coefficient between semi-infinite media denoted 1 and 2, with incidence coming from medium 1. r_{23} is similarly defined.
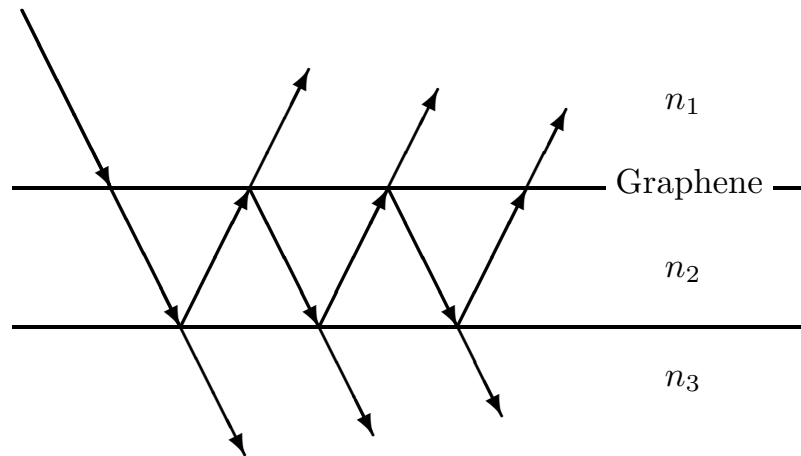

Fig. A.2. Schematic of graphene on quartz substrate, which makes up the air-graphene-quartz structure. n_1 and n_3 are the refractive index of air, n_2 that or quartz.
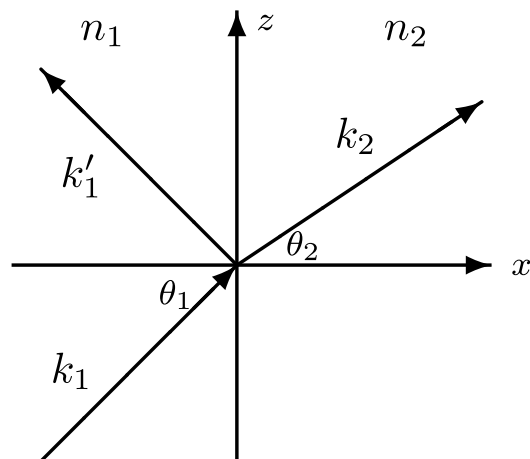

Fig. A.3. The plane interface between two semi-infinite regions of homogeneous media having refractive indices n_1 and n_2. Nonzero urface current density exists at the plane $x = 0$.

The presence of surface charge density leads to the boundary conditions

$$\hat{\mathbf{n}}_{12} \times (\mathbf{E}^{(2)} - \mathbf{E}^{(1)}) = 0 \qquad \hat{\mathbf{n}}_{12} \times (\mathbf{H}^{(2)} - \mathbf{H}^{(1)}) = \frac{4\pi}{c}\mathbf{j} \qquad (A.40)$$

A set of modified Fresnel coefficients were derived to incorporate the sheet conductance at the top interface, giving

$$
\begin{aligned}
t_{\text{TM}} &= \frac{2n_1 \cos\theta_1}{n_2 \cos\theta_1 + n_1 \cos\theta_2 + (4\pi/c)\sigma_s \cos\theta_1 \cos\theta_2} \\
r_{\text{TM}} &= \frac{n_2 \cos\theta_1 - n_1 \cos\theta_2 + (4\pi/c)\sigma_s \cos\theta_2 \cos\theta_1}{n_2 \cos\theta_1 + n_1 \cos\theta_2 + (4\pi/c)\sigma_s \cos\theta_2 \cos\theta_1} \\
t_{\text{TE}} &= \frac{2n_1 \cos\theta_1}{n_1 \cos\theta_1 + n_2 \cos\theta_2 + (4\pi/c)\sigma_s} \\
r_{\text{TE}} &= \frac{n_1 \cos\theta_1 - n_2 \cos\theta_2 - (4\pi/c)\sigma_s}{n_1 \cos\theta_1 + n_2 \cos\theta_2 + (4\pi/c)\sigma_s},
\end{aligned} \qquad (A.41)
$$

where n_1 and n_2 are the refractive indices of free space and quartz, respectively, and θ_1 and θ_2 are the angles between the wave vector and the interface normal in these two media, respectively.

Standard ellipsometer output Ψ and Δ are defined in terms of the ratio between TM and TE reflection coefficients, as follows

$$\frac{r_{\text{TM}}}{r_{\text{TE}}} = \tan\Psi e^{i\Delta}. \qquad (A.42)$$

The calculated averaged reflectance produce $\Psi_{\text{calc}}(\sigma_s)$ and $\Delta_{\text{calc}}(\sigma_s)$ [23,24], which is to be matched to the experimental quantities. We used the MATLAB [108] optimization toolbox to iteratively update the complex sheet conductivity in the model at each wavelength to match the experimental data.

B. THE T-MATRIX METHOD

We include a derivation of the transfer matrix method used in calculating the plane wave angle and wavelength-dependent power reflectance and transmittance of the graphene stacks. The transfer matrix relates the forward and backward propagating field components, $[E^+ \ E^-]^T$, at two different locations in the stratified structure [29]. Two types of matrices are present: a matrix $\mathbf{P}$ that describes propagation and a matrix $\mathbf{D}$ that imposes the boundary conditions [29]. $\mathbf{P}$ gives the plane wave phase retardation acquired over a homogeneous slab, and has the form

$$\mathbf{P}_i = \begin{bmatrix} e^{-ik_0 \cos\theta_i n_i d_i} & 0 \\ 0 & e^{ik_0 \cos\theta_i n_i d_i} \end{bmatrix}, \tag{B.1}$$

where n_i is the refractive index of the ith medium, d_i is the thickness, k_0 is the free space wavenumber, and θ_i is the angle between the wave vector and the surface normal. The $\mathbf{D}$ matrices impose the boundary conditions. Each boundary requires two $\mathbf{D}$ matrices to describe the tangential electric and magnetic field boundary conditions, as illustrated in Fig. B.1 and Fig. B.2.

Imposing the TE boundary conditions at the graphene boundary leads to

$$E_1 + E_1' = E_2 + E_2' \tag{B.2}$$

$$\sqrt{\frac{\varepsilon_1}{\mu_1}}(E_1 - E_1')\cos\theta_1 = \sqrt{\frac{\varepsilon_2}{\mu_2}}(E_2 - E_2')\cos\theta_2 + \frac{4\pi\sigma_s}{c}(E_2 + E_2'), \tag{B.3}$$

where the prime signifies the field associated with the $-x$-traveling waves, referring to Figs. B.1 and B.2. Equations (B.2) and (B.3) can be written as [29]

$$\mathbf{D}_1 \begin{bmatrix} E_1 \\ E_1' \end{bmatrix} = \mathbf{D}_{g2} \begin{bmatrix} E_2 \\ E_2' \end{bmatrix}, \tag{B.4}$$
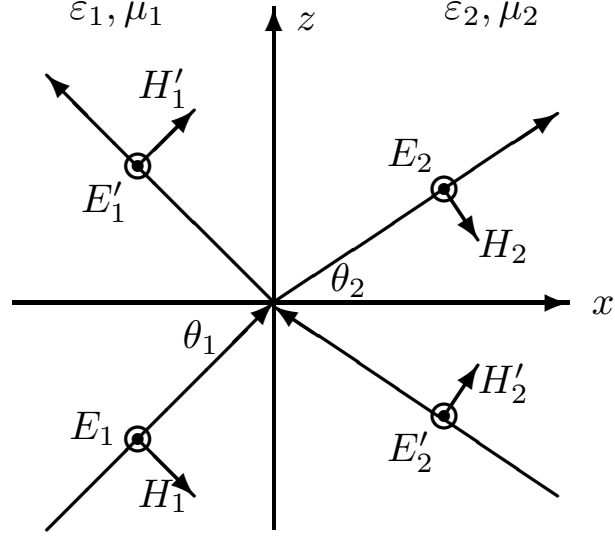
Fig. B.1. Reflection and transmission of TE waves. All components of electric field are directed out of the page.

where the subscript g indicates inclusion of the graphene sheet conductivity σ_s. Following from Eq. (B.4), the $\mathbf{D}$ matrices for medium i and TE-polarized waves are

$$\mathbf{D}_i = \begin{bmatrix} 1 & 1 \\ \sqrt{\frac{\varepsilon_i}{\mu_i}} \cos\theta_i & -\sqrt{\frac{\varepsilon_i}{\mu_i}} \cos\theta_i \end{bmatrix} \tag{B.5}$$

$$\mathbf{D}_{gi} = \begin{bmatrix} 1 & 1 \\ \sqrt{\frac{\varepsilon_i}{\mu_i}} \cos\theta_i + \frac{4\pi}{c}\sigma_s & -\sqrt{\frac{\varepsilon_i}{\mu_i}} \cos\theta_i + \frac{4\pi}{c}\sigma_s \end{bmatrix}. \tag{B.6}$$

Similar matrices can also be found for TM polarization (Fig. B.2). Applying boundary conditions on the tangential fields yields

$$(E_1 + E_1') \cos\theta_1 = (E_2 + E_2') \cos\theta_2 \tag{B.7}$$

$$\sqrt{\frac{\varepsilon_1}{\mu_1}}(E_1 - E_1') = \sqrt{\frac{\varepsilon_2}{\mu_2}}(E_2 - E_2') + \frac{4\pi}{c}\sigma_s \cos\theta_2 (E_2 + E_2'), \tag{B.8}$$

which gives

$$\mathbf{D}_i = \begin{bmatrix} \cos\theta_i & \cos\theta_i \\ \sqrt{\frac{\varepsilon_i}{\mu_i}} & -\sqrt{\frac{\varepsilon_i}{\mu_i}} \end{bmatrix} \tag{B.9}$$
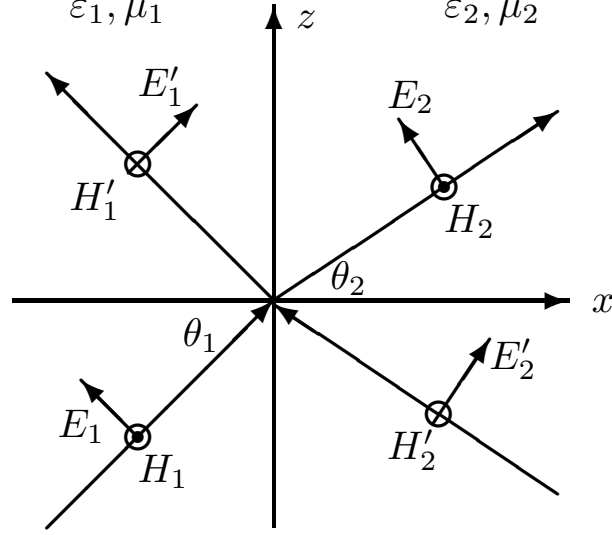
Fig. B.2. Reflection and transmission of TM waves. H_1 and H_2 are directed out of the page, and H_1' and H_2' into the page.

$$\mathbf{D}_{gi} = \begin{bmatrix} \cos\theta_i & \cos\theta_i \\ \sqrt{\frac{\varepsilon_i}{\mu_i}} + \frac{4\pi}{c}\sigma_s\cos\theta_i & -\sqrt{\frac{\varepsilon_i}{\mu_i}} + \frac{4\pi}{c}\sigma_s\cos\theta_i \end{bmatrix}. \tag{B.10}$$

The overall transmission matrix is a cascade of the $\mathbf{D}$ and $\mathbf{P}$ matrices for the entire stack, giving

$$\mathbf{M}_{\text{stack}} = \begin{bmatrix} M_{11} & M_{12} \\ M_{21} & M_{22} \end{bmatrix} = \mathbf{D}_0^{-1}\left(\mathbf{D}_i\mathbf{P}_i\mathbf{D}_i^{-1}\right)\left[\prod_{i=1}^{N-1}\left(\mathbf{D}_{gi}\mathbf{P}_i\mathbf{D}_i^{-1}\right)\right](\mathbf{D}_{gs}\mathbf{P}_s\mathbf{D}_s^{-1})\mathbf{D}_0, \tag{B.11}$$

where the subscript s represents substrate and N is the number of unit cells. Each unit cell is made up of one sheet of graphene and a dielectric spacer layer. In modeling stacks without substrate, the factor $(\mathbf{D}_{gs}\mathbf{P}_s\mathbf{D}_s^{-1})$ is omitted.

The reflectance is given by

$$R = \left|\frac{M_{21}}{M_{11}}\right|^2 \tag{B.12}$$

and the transmittance by

$$T = \frac{n_t\cos\theta_t}{n_i\cos\theta_i}\left|\frac{1}{M_{11}}\right|^2, \tag{B.13}$$

where n_1 is the refractive index of semi-infinite medium from which the incidence comes, and n_t that of the semi-infinite medium to which light is transmitted. In the case that $n_t = n_1$, such that they describe the same medium, e.g., free space, the transmittance simply reduces to $T = |1/M_{11}|^2$. We used Eqs. (B.12) and (B.13) to evaluate the plane wave reflectance and transmittance of the graphene stacks as a function of wavelength and incidence angle.

C. THE NICOLSON-ROSS-WEIR METHOD

The method we present was employed by A. Nicolson and G. Ross [92]. Here we make extensions to account for homogeneous background medium other than vacuum. Consider a slab structure situated within a homogeneous background characterized by permittivity ϵ_b.
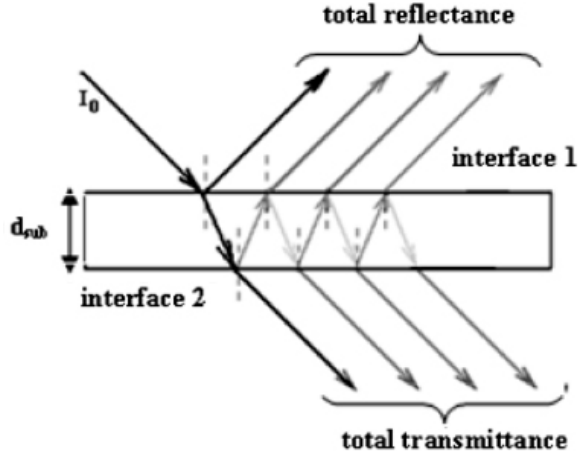
Fig. C.1. A slab of homogeneous material situated in some background medium

We let the slab be characterized by relative permittivity ϵ and relative permeability μ, and define $\eta = \sqrt{\mu/\epsilon}$. Correspondingly the background medium is characterized by relative permittivity and permeability ϵ_b, μ_b. We define $\eta_b = \sqrt{\mu_b/\epsilon_b}$.

If the slab were infinitely thick, we obtain the reflection coefficient at Interface 1 as

$$\Gamma = \frac{\eta - \eta_b}{\eta + \eta_b} \tag{C.1}$$

Consider a slab with finite thickness d. The transmission coefficient from the inner side of Interface 1 to the inner side of Interface 2 is simply the phase factor

$$z = \exp(i\omega\sqrt{\mu\epsilon}\,d) = \exp[i(\omega/c)\sqrt{\mu\epsilon}\,d] \tag{C.2}$$

From Eq. (C.1) and (C.2), the scattering coefficients from the slab may be obtained via Airy summation, which is the approach taken by A. M. Nicolson and G. F. Ross in [92].

$$S_{21} = (1 + \Gamma)z(1 - \Gamma) + (1 + \Gamma)z(-\Gamma)z(-\Gamma)z(1 - \Gamma) + \cdots$$

$$= \sum_{n=1}^{\infty} (1 + \Gamma)z^{(2n-1)}\Gamma^{(2n-2)}(1 - \Gamma)$$

$$= \frac{(1 - \Gamma^2)z}{1 - \Gamma^2 z^2} \tag{C.3}$$

$$S_{11} = \Gamma + (1 + \Gamma)z(-\Gamma)z(1 - \Gamma) + \cdots$$

$$= \Gamma + \sum_{n=1}^{\infty} (1 + \Gamma)z^{2n}(-\Gamma)^{2n-1}(1 - \Gamma)$$

$$= \frac{(1 - z^2)\Gamma}{1 - \Gamma^2 z^2} \tag{C.4}$$

Thus, we have managed to express the S-parameters in terms of the reflection coefficient Γ and the phase factor z.

C.1 Inverting the S-Parameters for z and Γ

The purpose of the inversion procedure is to obtain from Eq. (C.4) expressions of z and Γ in terms of S_{11} and S_{21}. In order to simplify the algebraic manipuation, we define the following two intermediate quantities, the sum and difference of the S-parameters,

$$V_1 = S_{21} + S_{11}, \tag{C.5}$$

$$V_2 = S_{21} - S_{11}. \tag{C.6}$$

C.1.1 Inverting for Γ

We can simplify the product of V_1 and V_2 as

$$
\begin{aligned}
V_1 V_2 &= (S_{21} + S_{11})(S_{21} - S_{11}) \\
&= S_{21}{}^2 - S_{11}{}^2 \\
&= \left[\frac{z(1 - \Gamma^2)}{1 - \Gamma^2 z^2}\right]^2 - \left[\frac{\Gamma(1 - z^2)}{1 - \Gamma^2 z^2}\right]^2 \\
&= \frac{z^2(1 - \Gamma^2)^2 - \Gamma^2(1 - z^2)^2}{(1 - \Gamma^2 z^2)^2} \\
&= \frac{z^2 - 2z^2\Gamma^2 + z^2\Gamma^4 - \Gamma^2 + 2z^2\Gamma^2 - z^4\Gamma^2}{(1 - \Gamma^2 z^2)^2} \\
&= \frac{z^2 + z^2\Gamma^4 - \Gamma^2 - z^4\Gamma^2}{(1 - \Gamma^2 z^2)^2} \\
&= \frac{z^2 - \Gamma^2 + \Gamma^2 z^2(\Gamma^2 - z^2)}{(1 - \Gamma^2 z^2)^2} \\
&= \frac{(z^2 - \Gamma^2)(1 - \Gamma^2 z^2)}{(1 - \Gamma^2 z^2)^2} \\
&= \frac{z^2 - \Gamma^2}{1 - \Gamma^2 z^2}
\end{aligned}
\tag{C.7}
$$

The difference between V_2 and V_1 is

$$
\begin{aligned}
V_1 - V_2 &= S_{21} + S_{11} - S_{21} + S_{11} \\
&= 2S_{11} \\
&= \frac{2\Gamma(1 - z^2)}{1 - \Gamma^2 z^2}.
\end{aligned}
\tag{C.8}
$$

Let

$$
X = \frac{1 - V_1 V_2}{V_1 - V_2}.
\tag{C.9}
$$

Using Eq. (C.7) and (C.8), we may simplify X as.

$$
\begin{aligned}
X &= \frac{1 - \frac{z^2 - \Gamma^2}{1 - \Gamma^2 z^2}}{\frac{2\Gamma(1 - z^2)}{1 - \Gamma^2 z^2}} \\
&= \left[\frac{1 - \Gamma^2 z^2 - z^2 + \Gamma^2}{1 - \Gamma^2 z^2} \right] \left[\frac{1 - \Gamma^2 z^2}{2\Gamma(1 - z^2)} \right] \\
&= \frac{1 - \Gamma^2 z^2 - z^2 + \Gamma^2}{2\Gamma(1 - z^2)} \\
&= \frac{1 - z^2 + \Gamma^2 - \Gamma^2 z^2}{2\Gamma(1 - z^2)} \\
&= \frac{(1 - z^2) + \Gamma^2(1 - z^2)}{2\Gamma(1 - z^2)} \\
&= \frac{(1 - z^2)(1 + \Gamma^2)}{2\Gamma(1 - z^2)} \\
&= \frac{1 + \Gamma^2}{2\Gamma}
\end{aligned}
\tag{C.10}
$$

From Eq. (C.10) we immediately obtain a quadratic equation in Γ,

$$
\Gamma^2 - 2X\Gamma + 1 = 0,
\tag{C.11}
$$

and we can solve for Γ in terms of the S-parameters,

$$
\Gamma = X \pm \sqrt{X^2 - 1},
\tag{C.12}
$$

since X is defined in terms of V_1 and V_2 which eventually depends on S_{11} and S_{21}.

C.1.2 Inverting for z

Obtaining z from the S-parameters is relatively straight-forward. It is easy to notice that

$$
\begin{aligned}
1 - \Gamma S_{11} &= \frac{1 - \Gamma^2 z^2 - \Gamma^2 + \Gamma^2 z^2}{1 - \Gamma^2 z^2} \\
&= \frac{1 - \Gamma^2}{1 - \Gamma^2 z^2}.
\end{aligned}
\tag{C.13}
$$

Since $S_{21} = \frac{(1 - \Gamma^2)z}{1 - \Gamma^2 z^2}$, we easily obtain

$$
z = \frac{S_{21}}{1 - \Gamma S_{11}}
\tag{C.14}
$$

Or, to make use of the intermediate quantities V_1 and V_2 we just defined, we notice that

$$
\begin{aligned}
V_1 &= S_{21} + S_{11} \\
&= \frac{(1 - \Gamma^2)z}{1 - \Gamma^2 z^2} + \frac{(1 - z^2)\Gamma}{1 - \Gamma^2 z^2} \\
&= \frac{(1 - \Gamma^2)z + (1 - z^2)\Gamma}{1 - \Gamma^2 z^2} \\
&= \frac{z - \Gamma^2 z + \Gamma - z^2 \Gamma}{1 - \Gamma^2 z^2}
\end{aligned}
\tag{C.15}
$$

$$
\begin{aligned}
V_1 - \Gamma &= \frac{z - \Gamma^2 z + \Gamma - z^2 \Gamma - \Gamma + \Gamma^3 z^2}{1 - \Gamma^2 z^2} \\
&= \frac{z - \Gamma^2 z - \Gamma z^2 + \Gamma^3 z^2}{1 - \Gamma^2 z^2} \\
&= \frac{(z - \Gamma z^2) + \Gamma z^2(-1 + \Gamma^2)}{1 - \Gamma^2 z^2} \\
&= \frac{(z - \Gamma z^2) - \Gamma z(z - \Gamma^2 z)}{1 - \Gamma^2 z^2} \\
&= \frac{(z - \Gamma z^2)(1 - \Gamma z)}{1 - \Gamma^2 z^2} \\
&= \frac{z(1 - \Gamma z)(1 - \Gamma z)}{1 - \Gamma^2 z^2}
\end{aligned}
\tag{C.16}
$$

$$
\begin{aligned}
1 - V_1 \Gamma &= 1 - \frac{(z - \Gamma^2 z + \Gamma - z^2 \Gamma)\Gamma}{1 - \Gamma^2 z^2} \\
&= \frac{1 - \Gamma^2 z^2 - \Gamma z + \Gamma^3 z - \Gamma^2 + \Gamma^2 z^2}{1 - \Gamma^2 z^2} \\
&= \frac{1 - \Gamma z + \Gamma^3 z - \Gamma^2}{1 - \Gamma^2 z^2} \\
&= \frac{(1 - \Gamma z + \Gamma^3 z - \Gamma^2)}{1 - \Gamma^2 z^2} \\
&= \frac{(1 - \Gamma z) + (\Gamma^3 z - \Gamma^2)}{1 - \Gamma^2 z^2} \\
&= \frac{(1 - \Gamma z) - \Gamma^2(1 - \Gamma z)}{1 - \Gamma^2 z^2} \\
&= \frac{(1 - \Gamma z)(1 - \Gamma^2)}{1 - \Gamma^2 z^2}
\end{aligned}
\tag{C.17}
$$

From Eq. (C.16) and (C.17), we observe that z can also be expressed as

$$z = \frac{V_1 - \Gamma}{1 - V_1 \Gamma} \tag{C.18}$$

C.2 Multiple Values and Ambiguities

The inversion of S-parameters doesn't produce unique results for the material parameters, due to the complex algebraic operation of taking the n-th roots of a complex number, where $n \in \mathbb{Z}$. In this subsection we focus on such operations. We list the places where they occur in the derivation, and present methods for overcoming these ambiguities to obtain uniquely determined wave and material parameters.

C.2.1 Multiple Values in Γ and z

We gather the inversion results obtained so far. Γ and z are respectively give in Eq. (C.12) and (C.18). z depends on Γ and hence all the ambiguities in Γ affect the results of z.

The solution for Γ in Eq. (C.12) contains the complex square root of the quantity $X^2 - 1$, which has two solutions and has been made explicit by writing the sign choice '$\pm$' in Eq. (C.12). The ambiguity is easy to remove, since there are only two solutions. We simply need to remove the one that is not physical, and select the solution that satisfies $|\Gamma| \leqslant 1$. This allows us to uniquely determine Γ. z is obtained by substituting Γ into Eq. (C.18). Thus we are able to uniquely determine Γ and z.

C.2.2 Multiple Values in Impedance and Wave Number

We show how ambiguity due to multiple values enters the expression for the wave number k, which is the worst difficulty in the application of the Nicolson-Ross-Weir method. Having obtained uniquely determined values of Γ and z, we can determine the intrinsic impedance $\eta = \sqrt{\mu/\epsilon}$ of the medium and the wave number k inside the medium.

We recall that

$$\begin{aligned}\Gamma &= \frac{\sqrt{\mu/\epsilon} - \sqrt{\mu_b/\epsilon_b}}{\sqrt{\mu/\epsilon} + \sqrt{\mu_b/\epsilon_b}} \\ &= \frac{\sqrt{\mu/\epsilon} - \sqrt{\mu_b/\epsilon_b}}{\sqrt{\mu/\epsilon} + \sqrt{\mu_b/\epsilon_b}}\end{aligned} \tag{C.19}$$

It is extremely easy to obtain

$$1 + \Gamma = \frac{2\sqrt{\mu/\epsilon}}{\sqrt{\mu/\epsilon} + \sqrt{\mu_b/\epsilon_b}} \tag{C.20}$$

and

$$1 - \Gamma = \frac{2\sqrt{\mu_b/\epsilon_b}}{\sqrt{\mu/\epsilon} + \sqrt{\mu_b/\epsilon_b}}. \tag{C.21}$$

Following the unique determination of Γ, there is no ambiguity with η. The wave number k is closely related to the phase factor z via $z = \exp(ikd) = \exp\left[i(\omega/c)\sqrt{\mu\epsilon}\, d\right]$.

$$k = \frac{1}{id} \ln(z) = -\frac{1}{id} \ln\left(\frac{1}{z}\right) \tag{C.22}$$

Equation (C.22), simple as it appears, leads directly to the most common difficulty associated with the Nicolson-Ross-Weir method. Mathematically, the complex logarithm produces infinitely many solutions [109]. For example, consider $w = |w|e^{i\theta}$.

$$\ln(w) = \ln|w| + i(\theta + 2\pi m), \tag{C.23}$$

where $m \in \mathbb{Z}$.

C.3 Choosing the Appropriate Solution

To eliminate the ambiguity arising from the effective refractive index n having multiple solutions, we need to settle on an appropriate choice of n, which could differ for different frequencies. The wave number k, as a function of frequency, should be continuous.

To sum up, in order to obtain unique values for η and k, we encounter two places where there are multiple values.

1. **The complex square root in Eq. (C.12)**. Since there are only two solutions, we simply need to choose the correct sign for the square root to ensure $|\Gamma| \leqslant 1$, to satisfy passivity.

2. **The complex natural logarithm in Eq. (C.22)**. This function produces an infinite number of choices, and poses the greatest challenge to the successful application of the Nicolson-Ross-Weir method. This requires S-parameter data at sufficiently low frequencies so that the phase progression over the thickness of the slab is less than 2π. If this cannot be realized, then there is a uniqueness problem in the selection of k, within modulo 2π. However, by using multiple incident angles at each frequency, it is in principle possible to circumvent this problem and obtain the unique material parameters. Furthermore, in an experiment, varying sample thicknesses may be possible, further aided unique extraction of the material properties.

Having settled the above two issues with multiple-valued functions, the values for η and k that we obtain are unique, with no ambiguities.

C.4 Obtaining ϵ and μ

With uniquely determined wave parameters η and k, it is quite straight-forward to obtain the material parameters ϵ and μ. We define the intermediate quantities c_1 and c_2 to simplify the expressions,

$$c_1 = \eta^2 = \frac{\mu}{\epsilon} = \left(\frac{1+\Gamma}{1-\Gamma}\right)^2 \frac{\mu_b}{\epsilon_b}, \tag{C.24}$$

$$c_2 = n^2 = \mu\epsilon = \left(\frac{k}{\omega/c}\right)^2 = -\left[\frac{c}{\omega d} \ln\left(\frac{1}{z}\right)\right]^2. \tag{C.25}$$

Following the definition, we obtain ϵ and μ as,

$$\epsilon = \sqrt{\frac{c_2}{c_1}}, \tag{C.26}$$

$$\mu = \sqrt{c_1 c_2}. \tag{C.27}$$

VITA

VITA

Mengren Man received his Bachelor of Engineering degree in Electrical and Electronic Engineering from Nanyang Technological University, Singapore, in 2010, with First Class Honours and a minor in applied physics. Since August 2010, he has been pursuing his Ph.D. in the School of Electrical and Computer Engineering at Purdue University, West Lafayette, IN, USA. His research involvement includes simulation and modeling in nanophotonics.